Superconducting Nanowire Single-Photon Detectors based on TaN Thin Films

---

Master Thesis

Mathematisch-naturwissenschaftliche Fakultät
der
Universität Zürich

Adrian Aeschbacher

Universität Zürich[UZH]

Dr. A. Engel
Prof. Dr. A. Schilling

Zürich
Oktober 2011

Abstract

Superconducting Nanowire Single Photon Detectors (SNSPD) are very fast, low noise devices, that detect single photons over a broad spectral range with practical quantum efficiency. The quantum efficiency drops at a certain deposited energy abruptly, the so called cutoff energy or the corresponding cutoff wavelength.

The most common material to fabricate these nanowires is niobium nitride (NbN). A promising material, that has not been used for this purpose before is tantalum nitride (TaN). Many material properties of TaN and NbN are similar, but TaN has a smaller energy gap. This should make the device more sensitive to photons with lower energies. In this thesis, SNSPDs made of NbN and TaN were characterized, the quantum efficiencies were measured and the cutoff criteria were determined and compared. With the use of TaN the cutoff wavelength could be increased significantly.

Measurements of quantum efficiency and dark-count rates at several temperatures and operation conditions are presented and discussed. Furthermore, the cutoff criteria are determined and compared between the materials mentioned as well as the experimental results are compared to the theoretical predictions of the detection model.

Contents

1 Introduction

In many scientific disciplines it is of great importance to detect photons with a high accuracy. In astronomy there is a need to detect very faint signals in the near to far infrared (IR) range [1]. Also time-resolved spectroscopy [2] or correlation spectroscopy [3] and various optical quantum information application, such as quantum key distribution [4], quantum communication [5] or (in the future) quantum computation application [6] share similar demands as well as single photon source characterization. The most essential properties are the ability to resolve single photons with high quantum efficiency (QE) and a low dark-count rate over a broad spectral range, a fast response time combined with a high counting rate as well as a low timing jitter.

To detect single photons, Photomultiplier Tubes (PMT) or Avalanche Photodiodes (APD) are used most commonly. PMTs show a very high QE, low dark-count rate and relatively high counting rate for visible light, but they are only sensitive to photons with a wavelength from approx. 115 nm to 1700 nm. Additionally for the detection of near infrared (NIR) photons their QE drops to a very low value and the dark-count rate rises substantially. [6]

APDs are only sensitive to single photons if they are used in the so called "Geiger-Mode", which means they are operated with a large reverse bias voltage above the breakdown voltage [2]. The spectral sensitivity of APDs for detecting single photons is restricted by the bandgap of the detection material. Si-APDs are only sensitive in the visible and very near IR range (approx. 400 nm to 1000 nm)[6]. In order to detect photons with a longer wavelength InGaAs is the material of choice. An InGaAs-APD is sensitive to photons with a wavelength of about 1000 nm to 1600 nm [6]. Such a detector operated in "Geiger-Mode" suffers from a relatively high dark-count rate. The higher the reverse bias voltage the higher the QE and the higher the dark-count rate. When cooled down to about 200 K a typical dark-count rate of such a device is a few kHz. [2]

A different approach for very sensitive light detection is based on superconductors (see section 2.2).

About ten years ago, a new principle of superconducting light detectors has been introduced [7]. These devices can be called "superconducting nanowire single photon detector" (SNSPD). They combine a practical quantum efficiency and low dark-count rate with a low jitter time and very high counting rate [8]. As the name suggests they are also sensitive to single photons. This would make them perfect candidates for the applications mentioned above and many more.

As a detecting material, niobium nitride (NbN) has proven to work very well, and most research in this field is focused on improving the performance of NbN-SNSPDs by means of integrating an optical cavity [5, 9] or adding anti-reflection coating [9] for example. But detectors made of other materials are also feasible. Some of them might even have better detection properties. A promising candidate is the chemically related compound tantalum nitride (TaN), which has not been used for this application before.

The material properties important for a photon detection are comparable to NbN or even favorable and the material is well suited for the nanoscale fabrication process.

The aim of this thesis is to characterize SNSPDs made of NbN and TaN and compare their detection properties.

2 Superconductivity

This is a very brief phenomenological overview about the aspects of superconductivity that are important for the operation principle of a SNSPD. It is in no way complete and the formalisms remain underived. For a profound treatment of this subject please refer to references [10] or [11] upon which the following section is based for the most part.

2.1 Overview

In 1911 Kamerlingh Onnes measured the resistance of mercury down to liquid helium temperature and discovered a jump of the resistance at a specific temperature. The measurement showed a decrease of the resistance to an unmeasurably low value. Later, permanent current-experiments suggested that the resistance is indeed zero or at least very close to zero.

Two years later Kamerlingh Onnes discovered that if a certain current is exceeded this effect vanishes. Later he found out that above a critical magnetic field strength superconductivity vanishes as well. F. B. Silsbee connected those two phenomena a few years later. In 1933 Meissner and Ochsenfeld discovered that if a subcritical magnetic field is applied to a superconductor the field is expelled from the interior of the superconductor, the superconductor acts as a perfect diamagnet ($\chi = -1$). The description of this so called "Meissner-Ochsenfeld-Effect" was possible by the development of the phenomenological London Theory. Fifteen years later Ginzburg and Landau succeeded in extending the London Theory in order to explain the behavior of a superconductor in a magnetic field in more detail. They took into account that the density of superconducting charge carriers can vary spatially by introducing a complex order parameter Ψ, which can be interpreted as the wavefunction of the quantum state of the superconducting charge carriers: $\Psi = \sqrt{n_s} \cdot e^{i\phi}$, where ϕ is the phase of the quantum mechanical wavefunction and $|\Psi|^2 = n_s$ the density of superconducting charge carriers.

Two of the most important results of Ginzburg and Landau were on one hand the existence of a length scale over which the order parameter Ψ and therefore the density of superconducting charge carriers n_s can vary. It is called the Ginzburg-Landau coherence length ξ_{GL}. On the other hand, they confirmed the results of the London theory that claims, that an external magnetic field can penetrate a superconductor up to the characteristic length λ_L, the London penetration depth. In the framework of Ginzburg and Landau, this parameter is often called the Ginzburg-Landau penetration depth λ_{GL}. Additionally the temperature dependence of those two parameters near the

critical temperature (T_c), that is the temperature at which the phase transition between normalconducting state and superconducting state occurs, was found to be the same [10]:

$$\xi_{GL}^2(T) = \xi_{GL}^2(0) \cdot \left(1 - \frac{T}{T_c(0)}\right)^{-1} \tag{1}$$

$$\lambda_{GL}^2(T) = \lambda_{GL}^2(0) \cdot \left(1 - \frac{T}{T_c(0)}\right)^{-1}. \tag{2}$$

More than four decades after the discovery of superconductivity, Cooper was able to show that due to interactions with the lattice ions, electrons can feel an attractive force and form a kind of a bound state. Those objects are called Cooper-pairs and were the basis for a complete theoretical framework that explained all observed phenomena to this time only one year later. This framework, developed by Bardeen, Cooper and Schrieffer, explains the conventional superconductivity and is called the BCS-Theory. Within this theory, the length ξ_0 is introduced as the "BCS-coherence length". It is the length scale over which the two components of a Cooper pair interact.

In the same year Abrikosov developed the theory of the so called type-II superconductors by applying the Ginzburg-Landau theory to superconducting alloys. He found that for type-II superconductors a magnetic field H_{c1} or a magnetic induction B_{c1} exists, above which the superconductor energetically favors its partial penetration by the magnetic field in the from of single flux quanta $\Phi_0 = \frac{h}{2 \cdot e}$, where h is the Planck constant and e is the absolute value of the electron charge. The so called vortices increase in number if the magnetic field H or the magnetic induction B is increased up to a critical value H_{c2} or B_{c2} above which the sample becomes completely normal conducting. Whether the superconductor favors the formation of vortices can be distinguished by looking at the Ginzburg-Landau parameter κ, which is defined as

$$\kappa = \frac{\lambda_{GL}}{\xi_{GL}}. \tag{3}$$

If $\kappa < \frac{1}{\sqrt{2}}$ the formation of vortices is energetically unfavorable compared to the expulsion of the magnetic field, the superconductor is of type I. If $\kappa \geq \frac{1}{\sqrt{2}}$ the formation of fluxlines is favored and the superconductor is of type II.

If the electron mean free path $l \ll \xi_0$, the superconductor is in the dirty limit. Because the substrate was only heated to approximately 700°C during deposition in our experiment, the resulting thin film is highly disordered which leads to a short mean free path in both materials used for this thesis. In the dirty limit the diffusivity of quasiparticles is [12]

$$D = -\frac{4k_b}{\pi e} \cdot \left(\left. \frac{dB_{c2}}{dT} \right|_{T \lesssim T_c(0)} \right)^{-1} \tag{4}$$

with k_B as the Boltzmann constant.

Using the diffusion coefficient D, the density of states at the Fermi-Level ($DOS(E_F)$) can be determined by the Einstein-Smoluchowski relation

$$DOS(E_F) = \frac{1}{e^2 \cdot \rho_n \cdot D}, \tag{5}$$

where ρ_n is the normal state resistivity and is calculated as

$$\rho_n = R_n \cdot \frac{A}{L} \tag{6}$$

where A is the cross section, L the length of the conductor and R_n the normal state resistance.

From the BCS-Theory it follows a simple relation to connect the critical temperature (T_c) and the energy-gap (Δ) [10]:

$$\Delta(0) = 1.76 \cdot k_B \cdot T_c(0). \tag{7}$$

This relation holds for weakly coupled superconductors. For strongly coupled superconductors the estimation for the energy gap has to be slightly modified from the BCS-like behavior. According to [13] the energy gap for NbN can be estimated by the experimentally determined relation

$$\Delta(0) = 2.08 \cdot k_b \cdot T_c(0). \tag{8}$$

According to [10] the exact GL-result for the second critical field is

$$\mu_0 H_{c2}^{GL}(T) = B_{c2}^{GL}(T) = \frac{\Phi_0}{2\pi \xi_{GL}^2(T)}. \tag{9}$$

From this ξ_{GL} can be determined. In most cases, the upper critical field is too high to be measured at temperatures close to zero. A possibility is to measure the critical field at several temperatures close to the critical temperature, where the critical field behaves linearly, and extrapolate it to T=0. In this way an approximation for the GL-critical field $B_{c2}^{GL}(T)$ is given by

$$B_{c2}^{GL}(0) = T_c \cdot \left. \frac{dB_{c2}}{dT} \right|_{T_c}. \tag{10}$$

In reality it has been shown that at low temperatures the upper critical field does not behave linearly any more and the linear extrapolation overestimates the second critical

field [14]. According to [14] this fact can be accounted for by multiplying the extrapolated field by a factor 0.69 (Werthammer's approximation). Like this, the second critical field can be determined by

$$B_{c2}(0) \approx 0.69 \cdot T_c \cdot \left.\frac{dB_{c2}}{dT}\right|_{T_c} \tag{11}$$

and analog to (9) an expression for the true coherence length (ξ) can be found

$$\xi(0) = \sqrt{\frac{\Phi_0}{2\pi B_{c2}(0)}}. \tag{12}$$

The temperature dependence of the true coherence length that includes the GL-dependence near T_c as well as approximates Werthammer's result for $T = 0$, can be approximated by [15]

$$\xi^2(T) = \xi^2(0) \left(1 - \frac{T}{T_c}\right)^{-1} \left(1 + \frac{T}{T_c}\right)^{-0.5}. \tag{13}$$

In the London Theory the London penetration depth is defined as [10]

$$\lambda_L = \sqrt{\frac{m}{\mu_0\, q^2\, n_s}}. \tag{14}$$

Here, m is the mass and q the charge of the charge carrier and μ_0 is the vacuum permeability.

For extremely dirty superconductors the magnetic penetration depth can be written as [12]

$$\lambda(0) = \sqrt{\frac{\hbar\, \rho_n}{\pi \mu_0 \Delta(0)}}. \tag{15}$$

The temperature dependence of the magnetic penetration depth in the extremely dirty limit is [11]:

$$\frac{\lambda(T)}{\lambda(0)} = \left[\frac{\Delta(T)}{\Delta(0)} \cdot \tanh\left(\frac{\Delta(T)}{2k_b T}\right)\right]^{-0.5}. \tag{16}$$

According to [15] this expression can be approximated by the much simpler expression

$$\frac{\lambda(T)}{\lambda(0)} = \left(1 - \left(\frac{T}{T_c}\right)^2\right)^{-0.5} \cdot \left(1 + \left(\frac{T}{T_c}\right)^{1.5}\right)^{-0.25}. \tag{17}$$

If dealing with thin films that can be treated as two dimensional ($d \ll \lambda$), the magnetic penetration depth has to be modified. According to [16] the effective penetration depth can be expressed as

$$\Lambda(T) = \frac{2\lambda^2(T)}{d}. \tag{18}$$

The effective penetration depth Λ is over 100 times larger than λ in the materials and geometries used for this thesis (see table 1 in section 5.1 and 2 in section 5.2) and exceeds the samples' dimensions at all temperatures. This allows us to assume a homogeneous current distribution [15]. With dimensions in the nanoscale and the material in the dirty limit the depairing critical current can be expressed as [15]

$$I_{c,d}(t) = \frac{2\sqrt{2\pi}\,\mathrm{e}^{2\gamma}}{21\zeta(3)\sqrt{3}} \cdot \frac{\Delta(0)^2}{\sqrt{k_B T_c(0)}} \cdot \frac{w \cdot d}{e\,\rho_n\sqrt{D\,\hbar}} \cdot (1-t^2)^{1.5} \cdot (1+t^2)^{0.5} \tag{19}$$

where t is the reduced temperature, $t = \frac{T}{T_c}$, $\zeta(3) = 1.202$ is Apery's constant and $\gamma = 0.577$ is Euler's constant. The experimental critical-current, that can be determined from an I-V-characteristic for example, will typically be smaller than this theoretical value (see section 5.4) for a number of reasons.

2.2 Superconducting Light Detectors

There are two kinds of superconducting detectors: thermal equilibrium detectors and pair-breaking detectors. One example for each is given here.

A TES is basically a very sensitive bolometer. The very steep rise in the electrical resistance of a superconductor at the transition temperature at a given bias current is used to detect very small changes in temperature induced by a photon or a charged particle. Those detectors are sensitive to single photons, have a low dark-count rate, a large spectral range and high quantum efficiency, but the maximal count rate is limited to about 100 kHz [6]. For more information about TES please refer to Refs. [17] and [18].

As an example of a pair-breaking detector, Superconducting Tunnel Junctions (STJ) shall be mentioned briefly. A STJ consists of two superconducting electrodes separated by a thin insulating layer biased with a constant voltage. The photon is absorbed in one of the electrodes and breaks a Cooper-pair. The excited electron loses energy by breaking other Cooper-pairs leading to a quasiparticle multiplication. The resulting quasiparticles tunnel through the insulator into the second electrode. The tunnel current is a measure of the energy absorbed. STJ have a very high quantum efficiency but a low maximal count rate of 10 kHz to 100 kHz [19]. For more information about STJ, please refer to Refs. [19] and [20].

3 Superconducting Nanowire Single Photon Detector (SNSPD)

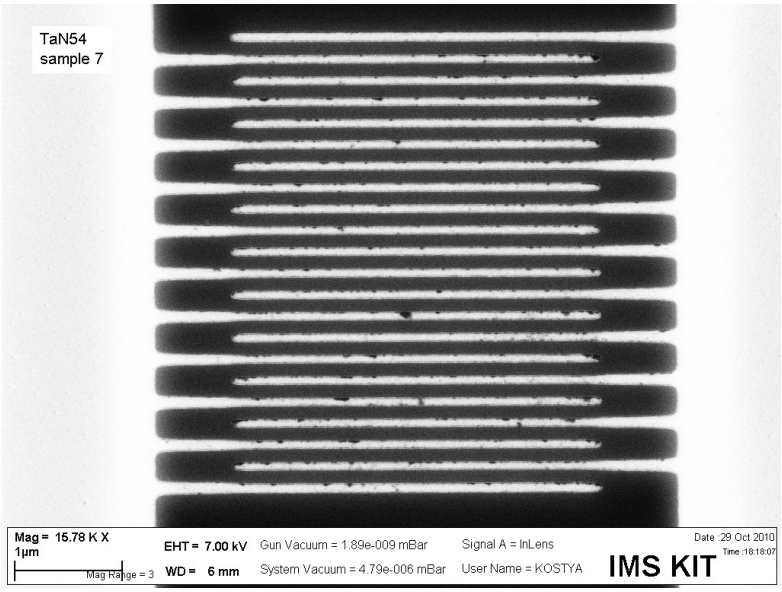

Figure 1: SEM picture of the TaN-SNSPD used. The nanowire is 126 nm wide and covers 63% of the $3.4\,\mu\text{m} \times 4.2\,\mu\text{m}$ area.

About ten years ago a novel kind of superconducting photon detector was proposed by Semenov et al. [7]. It is a superconducting nanowire structured from a thin film which is grown on a sapphire substrate. The wire is structured as a meander line in order to cover a large area. Figure 1 shows a SEM picture of the TaN-SNSPD used in this thesis. The dimensions are mentioned in table 1 in section 5.1. The thickness d of the wire is chosen to be on the order of ξ_{GL}. The small thickness of the wire results in a large effective penetration depth Λ (see Eq. (18)), that exceeds the line width w of the wire even at very low temperatures.

These dimensions in the nanometer scale enable a detection mechanism which will be described in the following section.

3.1 Detection Model

The detection mechanism was published in [21] and the following remarks are based on this publication.

Figure 2 illustrates a part of the nanowire. The line width w is much larger than the thickness d. This allows one to treat the diffusion of quasiparticles as a two-dimensional problem. During operation the nanowire is biased with a current driven by a constant

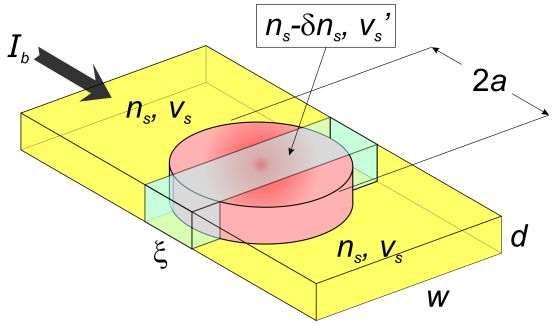

Figure 2: Scheme of the nanowire carrying a bias current I_b. After the photon is absorbed the quasiparticle cloud has spread (red). The volume relevant for froming a resistive domain (the "ξ-slab") is marked green.

voltage. Due to the meander geometry the magnetic field generated by the supercurrents can be neglected, and in the absence of any magnetic vortices the density of the superconducting charge carriers n_s should be constant across the strip width of the nanowire. The density of superconducting charge carriers can only vary over a distance ξ or larger along the current path. In figure 2 the relevant volume for changes in the density of superconducting charge carriers is indicated ("ξ-slab"). It is confined by the nanowire's thickness, its width and ξ.

When a photon is absorbed in the nanowire, the energy deposited breaks a Cooper-pair. This leads to an excited electron which loses its energy via electron-electron or electron-phonon interactions. This thermalization process happens on a time scale that is the thermalization time τ_{th} and will break other Cooper-pairs leading to an avalanche-like multiplication process that generates a cloud of quasiparticles. This mechanism is illustrated in figure 3. The thermalization time for thin NbN films has been measured to be τ_{th}=7 ps [7]. We are not aware of any measurements of τ_{th} for TaN films. Therefore the time constant was assumed to be the same for TaN thin films. After a time $t \geq \tau_{th}$ the electrons have thermalized to the energy level Δ. The amount of broken Cooper-pairs, as a theoretical maximum, is given by the energy deposited in the superconductor ($h\nu$) and the energy gap (Δ). In reality this process is not completely efficient. This is accommodated by the experimental factor β that ranges between 0 and 1 and shall be called the quantum yield. The number of quasiparticles $M(t)$ reaches a maximum in the "ξ-slab" after τ_{th} and is therefore given by

$$M(\tau_{th}) = \frac{h\nu}{\Delta}\beta. \tag{20}$$

The photon is absorbed in the nanowire reducing the number of Cooper-pairs $n_s^{'} = n_s - \delta n_s$. The quasiparticles diffuse from the photon absorption site creating a so called hot-spot. The concentration of quasiparticles can be calculated solving the two-dimensional

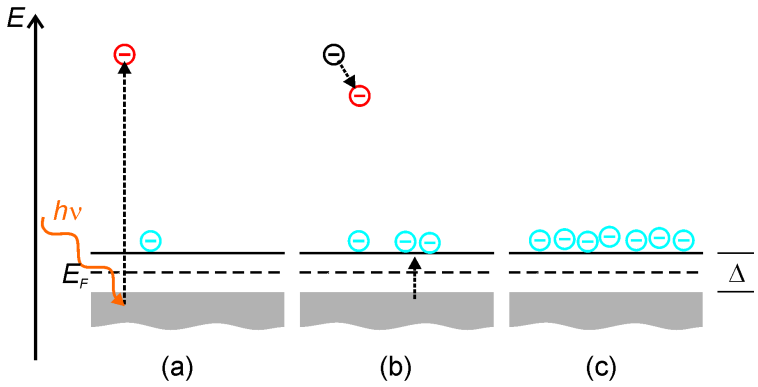

Figure 3: Sketch of the photon absorption and quasiparticle multiplication process in the semiconductor model. (a): The photon is absorbed breaking a Cooper pair which leads to an excited electron. (b): The excited electron loses energy via electron-electron and electron-phonon interaction breaking other Cooper-pairs while relaxing. (c): After a certain time all excited electrons have relaxed to the energy level Δ.

diffusion equation. The result is the concentration of quasiparticles, due to multiplication and diffusion dependent on position and time

$$C(r,t) = \frac{M(t)}{4\pi D\, d\, t} \exp\left(-\frac{r^2}{4D\, t}\right). \tag{21}$$

The local supercurrent density can be associated with the local density of superconducting charge carriers n_s and their velocity v_s as $j_s = e \cdot n_s \cdot v_s$ and accordingly the critical current-density

$$j_c = e \cdot n_s \cdot v_c. \tag{22}$$

As mentioned before, the local supercurrent density is constant in the "ξ-slab" of the nanowire marked in figure 2. Due to charge flow conservation, the reduction of the superconducting charge carriers leads to to an increased pair velocity:

$$v_s' = \frac{n_s}{n_s - \delta n_s} v_s. \tag{23}$$

The "ξ-slab" switches in the normal state if the pair velocity v_s' exceeds the "critical velocity" v_c.

Given the assumption that for low enough temperatures ($T < \frac{T_c}{2}$) the approximation

$$n_s \approx DOS(E_F) \cdot \Delta \tag{24}$$

is valid, using (22), (23) and (24) one can calculate the minimal number of quasiparticles needed in order to switch the "ξ -slab" in the normal state as

$$\delta N^* = DOS(E_F)\Delta\, w\, d\, \xi \left(1 - \frac{I}{I_c}\right). \tag{25}$$

Since the quasiparticle cloud evolves very quickly, its radius exceeds ξ long before τ_{th} and not all quasiparticles in the cloud contribute to the reduction of Cooper-pairs in the volume of interest, but only the ones in the "ξ-slab". Integrating the quasiparticle concentration (21) over this volume gives the number of relevant quasiparticles as

$$\delta N = \frac{M(t)\xi}{\sqrt{\pi D t}}. \tag{26}$$

Equating (25) and (26) at $t = \tau_{th}$, using the relation in Eq.(20) allows to write down an expression for the minimal energy needed to trigger a counting event. This energy limit is referred to as the cutoff energy ϵ_{cutoff} and the corresponding cutoff wavelength λ_{cutoff},

$$\varepsilon_{\text{cutoff}} = \frac{hc}{\lambda_{\text{cutoff}}} = \frac{DOS(E_F)\Delta^2 w d\sqrt{\pi D \tau_{th}}\left(1 - \frac{I}{I_c}\right)}{\beta}. \tag{27}$$

If the operation conditions are chosen in a way that the energy of an arriving photon is above the cutoff energy, the photon is counted with a probability only limited by the absorption probability. A photon with an even higher energy is counted with the same probability. For a perfectly uniform nanowire the quantum efficiency is independent of the photon energy above the cutoff energy, the absorbability of the thin nanowire is the limiting factor. That means the detector is in the state of saturation.

In summary, the absorbed photon reduces the local critical-current density that is exceeded by the bias current, leaving a resistive domain which leads to a short voltage pulse. The detection of less energetic photons is less efficient and underlies a different detection mechanism.

3.1.1 Detection of Photons Beyond the Cutoff

The detection of a photon with an energy below the cutoff energy is of a different nature than the detection discussed above, and the exact detection principle is still under discussion. According to [15] and [22] the photon energy could assist the thermal fluctuation in the nanowire which leads to a counting event. The study of fluctuations in SNSPDs were not in the scope of this thesis and therefore will only be discussed very briefly. For a more detailed treatment of this subject please refer to Refs. [15] and [22].

In [15] and [22] the authors propose as fluctuation mechanisms, the unbinding of vortex-antivortex pairs (VAP) and in the overcoming of an energy barrier by a vortex, both in agreement with experimental data.

Unbinding of Vortex and Antivortex Pairs In this scenario all thermally excited vortices will be paired for temperatures smaller than a characteristic temperature. The application of a bias current exerts a Lorentz force and pulls the pair apart, thus lowering the energy of the VAP. The lowered binding energy of a VAP may be overcome by a thermal excitation and the vortex and the antivortex start moving in opposite directions dissipating energy which initiates the formation of a normal conducting domain. A photon with an energy below the cutoff energy may increase the probability of such an event.

Vortex Hopping over the Edge Barrier The entry of vortices at the edge of a superconductor is only suppressed by an edge barrier, similar to the Bean-Livingston-barrier for pinning vortices to the surface. Once overcome this barrier, a vortex will start moving across the strip perpendicular to the bias currents direction and release heat that creates a normal conducting domain similar to scenario of VAPs. A photon may increase the probability of a vortex hopping over the barrier, leading to a counting event.

In both scenarios the quantum efficiency decreases nearly exponentially with increasing photon wavelength.

4 Experimental Setup

The experimental setup is shown in figure 4. It can be divided into three main parts:

- Cryogenics
- Electronics
- Optics

Each part will be described in the following sections.

4.1 Cryogenics

4.1.1 Cryostat

We used an optical ^{3}He-cryostat manufactured by Janis Research Company. Figure 5 shows a schematic drawing of the cryostat, where the most important parts for operation are labeled. The He reservoir is enclosed by vacuum. This insulation vacuum is achieved with a turbopump together with a rotary vane pump and reaches around 10^{-5}mbar before transferring liquid helium. When the He-tank is filled with liquid helium, the entire wall of the tank acts as a cryogenic pump and the pressure of the insulation vacuum decreases further to around 10^{-8}mbar. To reduce black body radiation from

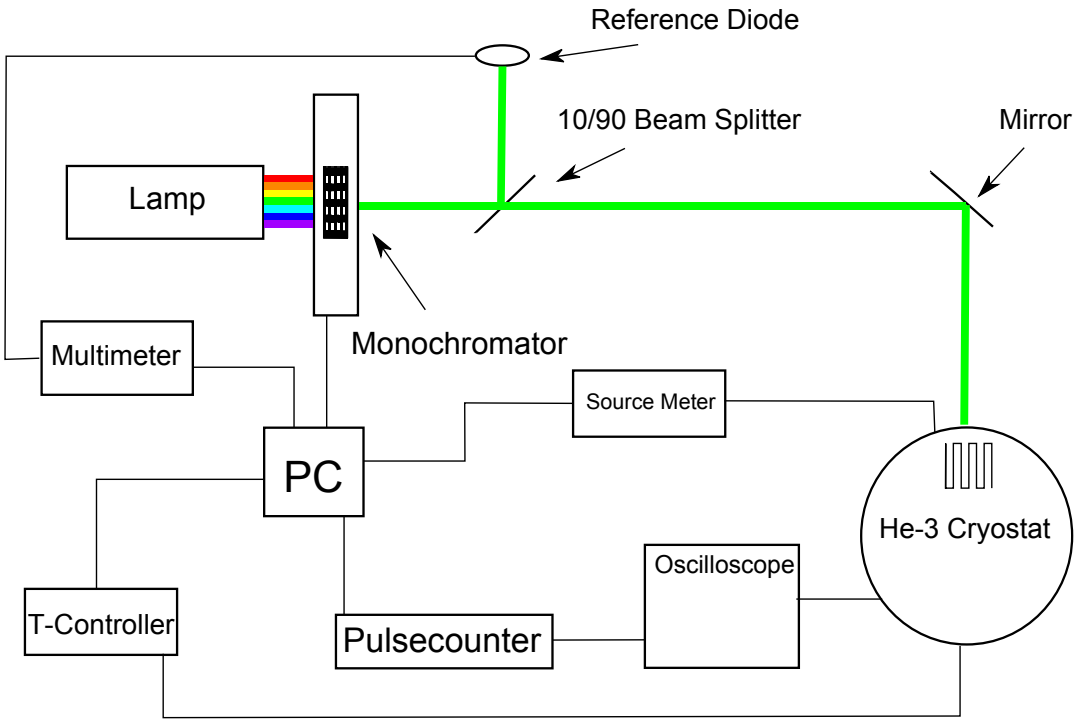

Figure 4: Schematic sketch of the experimental setup that is discussed in the main text. The light emitted from the arc-discharge lamp enters the monochromator where it is dispersed. A single wavelength leaves the monochromator and is directed onto the SNSPD. All devices are connected to a PC and are controlled by a Labview software.

outside the cryostat, the He reservoir is shielded by a LN_2 reservoir which again is insulated by vacuum against room temperature. The heat-shields at the bottom of the cryostat are thermally coupled to the respective reservoir. At the position where the sample holder and the sample are mounted there are optical openings on two sides. This allows to expose the sample to light. The openings can be closed either by aluminum disks or quartz glass windows. If the sample is exposed to light, a series of apertures minimize the heat flow into the cryostat.

The working principle of this ^{3}He-cryostat is outlined in the following. For the location of the described part consult figure 5.

The liquid helium is pushed from the reservoir through a capillary into the 1K-pot. The flow can be controlled with a needle valve from the top of the cryostat. The pressure in the 1K-pot is reduced using a rotary vane pump, typically to a few mbar. Under reduced pressure more helium evaporates and the latent heat cools the 1K-pot. Adjusting the needle valve carefully, one can find a setting where exactly as much liquid helium is drawn from the reservoir through the capillary as is evaporated. This way a typical temperature of approximately 1.6 K is reached in the 1K-pot. The ^{3}He system, that allows to reach temperatures below 1 K, is located in the center of figure 5. Contrary to the ^{4}He system, the ^{3}He system is a closed-cycle system. The storage vessel is mounted on top of the cryostat (in figure 5 only the inlet is shown) and connected to the charcoal which again is connected via a steal tube to the ^{3}He-pot. The charcoal can be either heated with a heater controlled by the temperature controller or be cooled by letting evaporated He-gas flow around it. It acts as a cryo-sorption pump for ^{3}He. When cooling down the sample, the charcoal has to be heated to approximately 45 K, ensuring no ^{3}He is adsorbed in the charcoal. The steal tube runs from the charcoal through the 1K-pot. At temperatures below approximately 2 K ^{3}He starts condensing, which leads to a microfilm of ^{3}He along the inside of the steal tube, thermally connecting the 1K-pot and the ^{3}He-pot. Keeping the 1K-pot at very low temperature macroscopic amounts of ^{3}He condense and drip into the ^{3}He-pot. After most of the ^{3}He has condensed, one can start to pump at the ^{3}He-pot using the charcoal-cryo pump by switching off the heater and cool it down. ^{3}He atoms will start to evaporate cooling down the ^{3}He-pot.

With ideal conditions we reach a temperature as low as 500 mK in steady operation for approximately three hours.

4.1.2 Temperature Control

An accurate and precise temperature measurement and control is one of the key factors for this experiment. We used a variety of temperature sensors at different positions in the cryostat not only to observe the sample temperature, but also to get an insight of what is happening in the cryostat.

Heart of the temperature control is the LakeShore Temperature Controller 340, a device that measures and displays temperatures and controls two PID loops with either

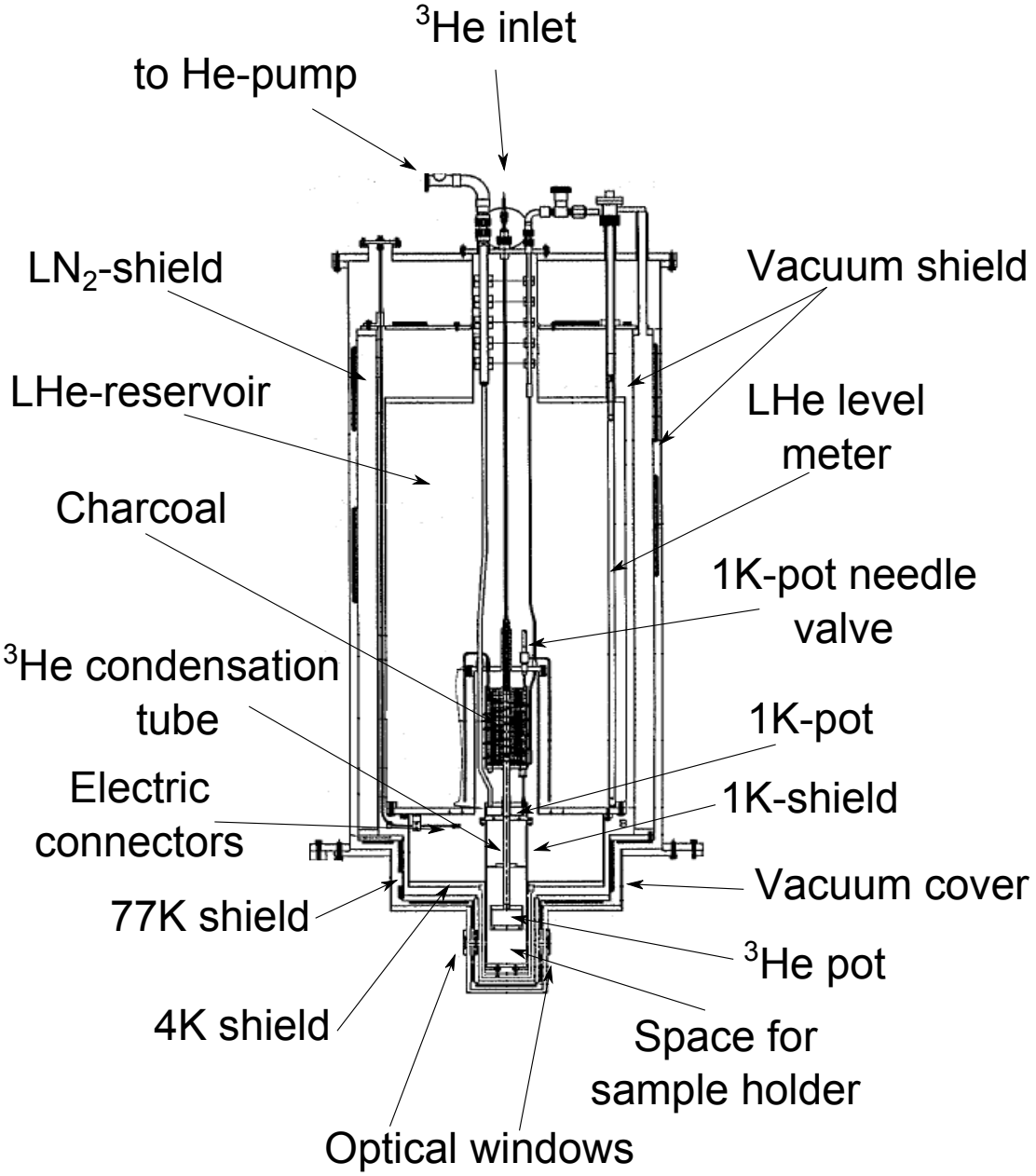

Figure 5: Drawing of the ^{3}He cryostat. See main text for the operation principle and the description of the individual parts.

an internal or external power source.

One heating loop is used to stabilize the sample temperature. This heater is attached to the ^{3}He-pot, but it uses the sample's temperature as a reference. The other heater loop controls the temperature of the charcoal that is used as a sorption pump.

We use five thermometers to observe the experiment. To determine the temperature of the charcoal and the 1K-pot two silicon temperature sensors are used, at the ^{3}He-pot a rubidium oxide sensor is used. To determine the sample temperature a thin film Cernox sensor is mounted onto the sample holder directly next to SNSPD-chip. All these sensors are read out by the temperature controller. When cooling down the cryostat, it can be interesting to know the temperature of the LHe tank. It can indicate if there is any liquid nitrogen left in the tank (when precooling with LN_2), or when transferring LHe at LN_2-temperature, whether the He is condensing. For that purpose a Pt-100 sensor is attached to the outside of the LHe tank since a precise temperature determination is not necessary for this thermometer.

During the measurements the temperature was held stable with maximal fluctuations of $\pm$ 10 mK.

4.2 Electronics

The scheme for the electronic setup is shown in figure 6. The chip containing the SNSPD is mounted directly on the sample holder to ensure a good thermal contact. Next to the chip, a printed circuit board is screwed down on the sample holder containing a part of the cryo-electronics. The contact pads on the SNSPD-chip are bonded to the contact pads of the printed circuit board. The sample holder is shown in figure 7. On the right hand side are the connectors for the sample thermometer. The thermometer itself is mounted on the sample holder right next to the SNSPD-chip.

The bias voltage is generated with a Keithley Source Meter 2410 that could be controlled by a labview software. The voltage is brought to the cryostat with a coaxial cable and passes through a low-pass filter to diminish electronic noise. In the cryostat, the voltage passes through another low-pass filter that is part of the printed circuit board, and reaches the contact pads that are bonded to the SNSPD-chip.

The pulse signal is picked up from the sample holder with a mini-coaxial cable, passes through a signal inverting cryogenic amplifier with a bandwidth of 40 MHz to 1.9 GHz and is brought outside the cryostat. From there, a semirigid coaxial cable passes the signal through a $-$3dB attenuator to a second amplifier. The $-$3dB attenuator damps reflections between the two amplifiers and prevents the formation of a standing wave. After the second amplifier the signal is damped by $-$6dB before it reaches the oscilloscope. Before the signal cable enters the oscilloscope or the pulse counter, a not terminated about 310 mm long coaxial cable, that acts as a notch filter is attached using a tee-piece connector to reduce some noise of unknown origin around 240 MHz.

Since the connections run from the laboratory (300 K) into the cryostat to the sample

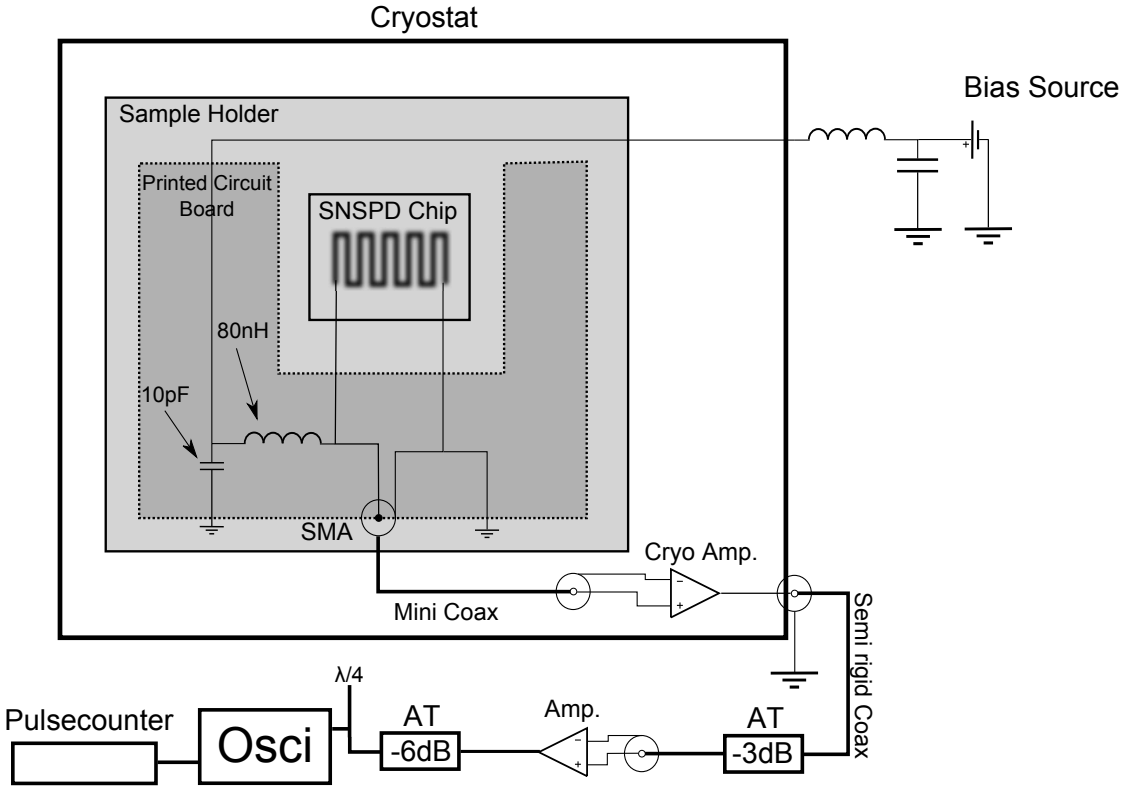

Figure 6: Schematic sketch of the electronic setup. The printed circuit board is mounted on the sample holder next to the SNSPD-chip. The bias voltage passes two low-pass filters before it reaches the SNSPD. The pulse signal is amplified twice, a first time inside the cryostat and a second time outside the cryostat. In between the signal is damped to reduce reflections. The parts are described in the main text. For the sample holder see also figure 7.

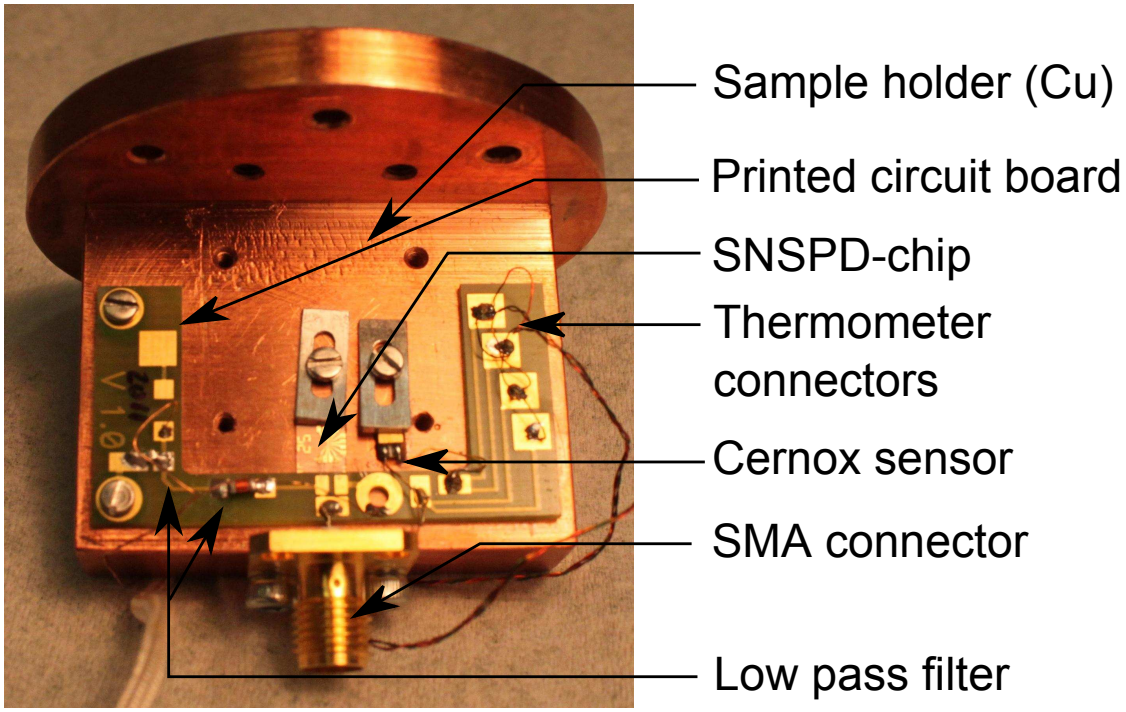

Figure 7: Picture of the sample holder. The printed circuit board, the SNSPD-chip and the Cernox thermometer are mounted.

(∼0.5 K), extra care has to be taken, when choosing the cables. On the one hand the cables should be bad thermal conductors in order to keep the heat flow into the cryostat as small as possible, on the other hand good electrical conductors are needed to reduce Joule heating. The choice of the cables is often a trade off. For the pulse signal a carbon steal semirigid coaxial cable manufactured by Lake Shore Cryotronics is used. The cable is thermally anchored at several points. At the end of the cable, where it is connected to the SMA-connector of the sample holder, a semirigid copper coaxial lead is used to reduce stress on the cable and the plug. Due to the dramatic change of the heat capacity at very low temperatures, it can make sense to use different kinds of cables at different temperature stages in the cryostat. To transport the bias current from the cable entry at the top of the cryostat to the 4 K-region, a low thermal conductance coaxial cable is used. From the 4 K-region a 50 μm thick twisted pair manganin cable leads the current to the sample holder. The Cernox temperature sensor is connected from room temperature to the 4 K-region by a 50 μm manganin cable. From there, a Quad-Lead Cryogenic Wire by Lake Shore Cryotronics is used.

Figure 8 shows a typical voltage pulse caused by a 300 nm-photon in the NbN-SNSPD, recorded at 500 mK with a bias current of 89% of the critical current. The first negative peak is the actual photon response caused by the formation of the resistive domain. Its amplitude depends on the applied bias current and the pulse rise time is well below 1 ns. The first positive peak stems from the charge stored in the capacity of the capacitor of the low-pass filter on the printed circuit board and the coaxial cable. Then, the oscillation is damped and reaches noise level after about 30 ns with this electronic setup. The impedance of the mini-coaxial cable that picks up the signal from the sample holder differs a little from 50 Ω. That leads to partial reflections of the AC-signal at the cryogenic amplifier which has an impedance of 50 Ω. Since the impedance of the electronics on the printed circuit board differs significantly from 50 Ω the reflected signal is reflected once more, resulting in the spiky features that can be seen in the second positive peak of the pulse.

The events were counted by a SR 400 Gated Photon Counter with a bandwidth of 200 MHz manufactured by Stanford Research Systems. The counter was equipped with an internal discriminator to set a trigger level on the counting events. The ideal setting of the discriminator level had to be estimated before each measurement by scanning through a spectrum of discriminator levels (−300 mV to +300 mV). At low discriminator levels the counter counts all kinds of noise signals, at high discriminator levels the counter does not count at all. In between one should observe a plateau, which means that the first maximum triggers the counter, but the following peaks of the pulse do not, the count rate is independent of the discriminator level. Figure 9 shows a measurement of the pulse-counter's count rate as a function of the discriminator level using the NbN-SNSPD exposed to 550 nm light at a temperature of 1.9 K. Setting the pulse counter to trigger on the negative amplitude, a plateau can not be observed. If the discriminator level is set to a positive amplitude, a plateau is clearly visible.

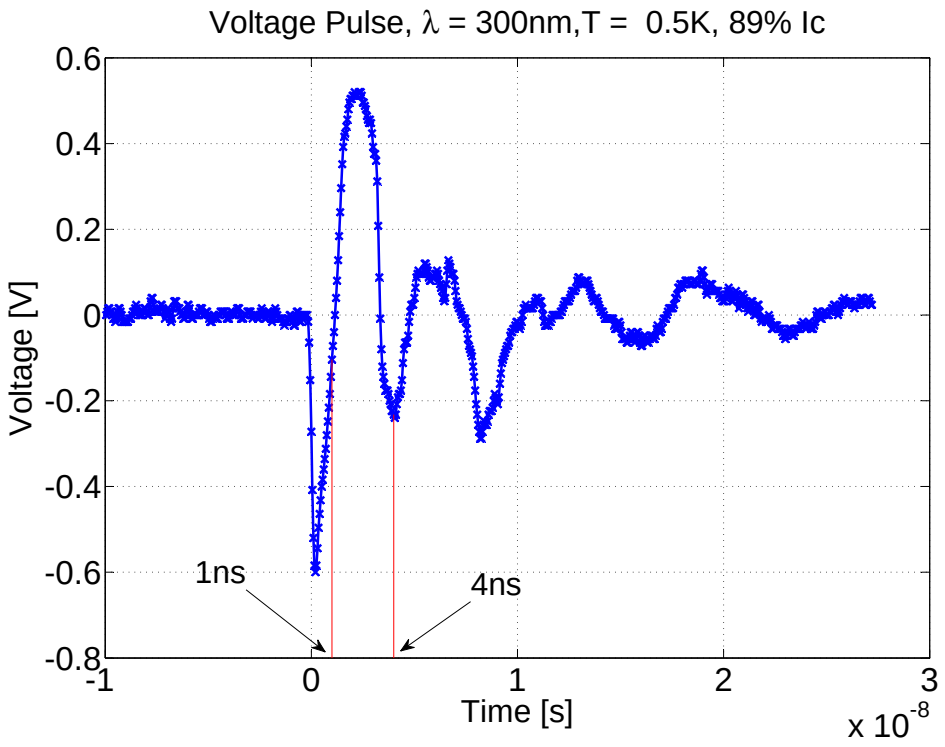

Figure 8: Voltage pulse caused by a single 300 nm-photon in a NbN-SNSPD recorded at 500 mK with a reduced bias-current $\left(\frac{I_b}{I_c}\right)$ of 0.89. The first negative peak is the signal of the formation of the resistive domain, followed by a electronic feedback from the capacities of the cables and electronic components. After only 4 ns the signal starts dying out. See main text for a more detailed discussion.

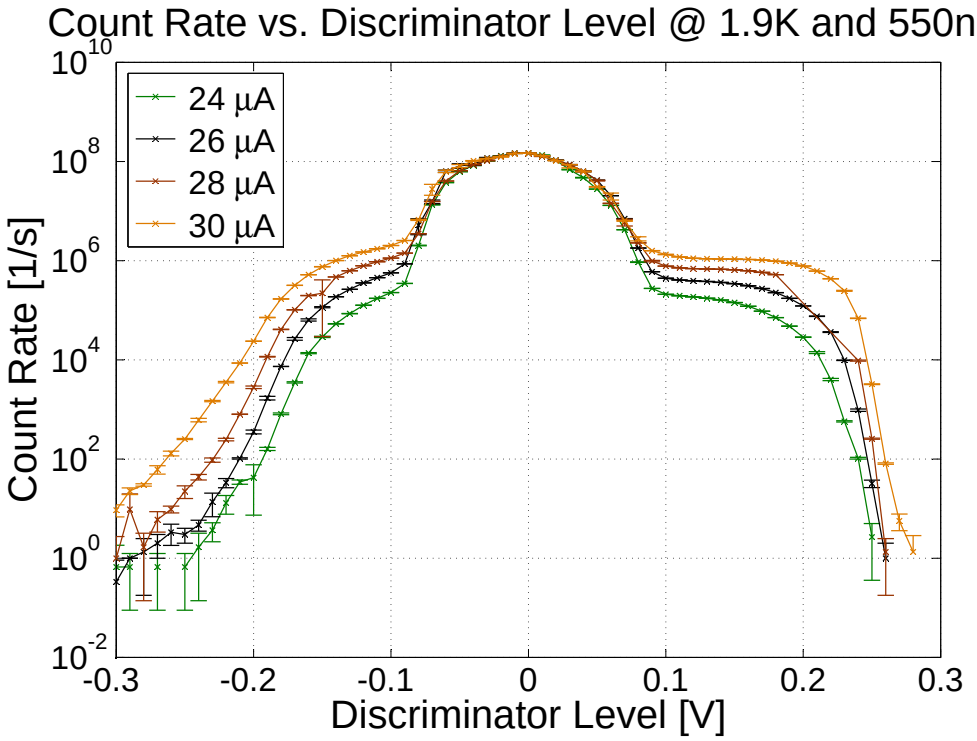

Figure 9: Count-rate dependence on the discriminator level of the pulse counter at different bias currents. At positive discriminator levels a plateau can be identified. The values in the plateau are reasonable choices for the discriminator level.

4.3 Optics

4.3.1 Light Source

As a light source we used a Newport Monochromator Illuminator with a 75 Watt Xenon arc-lamp together with a Cornerstone Diffraction Grating Monochromator, giving us access to a broad spectrum from 200 nm to 2500 nm. With the lamp used and the optical setup, a practical intensity could only be reached for wavelengths above 300 nm.

Figure 10 shows the operation principle of the grating monochromator schematically. The light enters the monochromator and is deflected onto a concave mirror. The mirror focuses the light on the diffraction grating, where it is deflected and reflected back to the concave mirror. The dispersed light is focused and deflected to the exit slit. The wavelengths are spatially separated and are moved over the exit slit by turning the grating. This monochromator holds two different diffraction gratings that can be changed automatically. The wavelength at which the grating is changed can be chosen within a certain limit. It was set to 1000 nm. To avoid overlapping orders of diffracted light, the lamp is equipped with a motorized filter wheel. The monochromator is able to communicate with the lamp's filter wheel, ensuring the correct filter is used automatically.

The monochromator is controlled with a PC using either a software provided by the manufacturer or with an appropriate Labview software.

4.3.2 Optical Setup

In figure 11 the optical setup is shown and the optical path is indicated. The beam splitter reflects 10% and transmits 90% of the light's intensity. The reflected beam is focused on the reference diode by a convex lens. The transmitted beam is deflected by a mirror, passes through a convex lens and finally reaches the SNSPD. For an illumination as homogeneous as possible the SNSPD is placed a little bit out of focus.

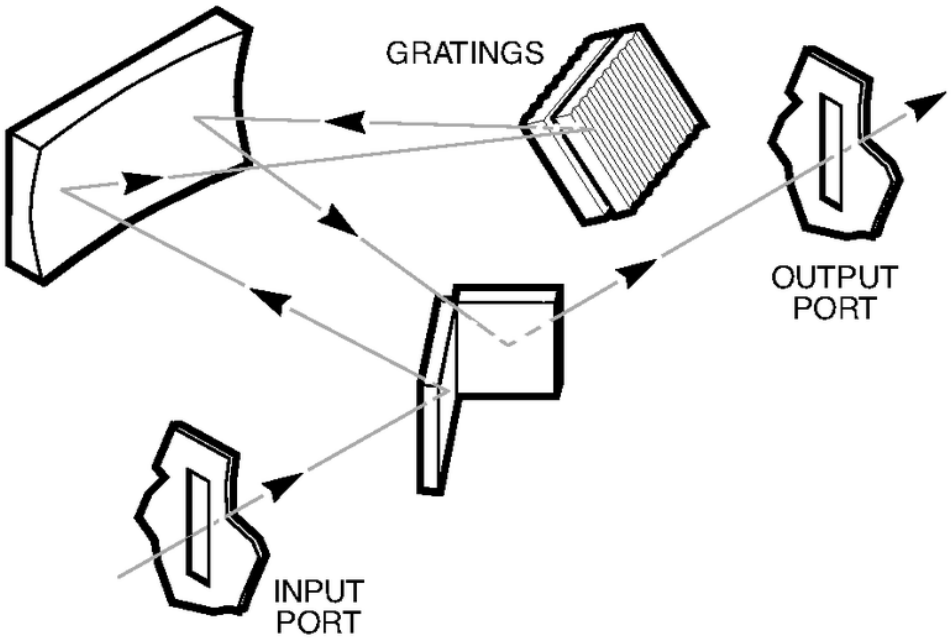

Figure 10: Schematic sketch of the working principle of a grating monochromator. The incoming light is directed onto a concave mirror that focus the light on the grating. From there the dispersed light is reflected back to the concave mirror that focus the light on the output port. By turning the grating the wavelength that exits the output port can be selected. [23]

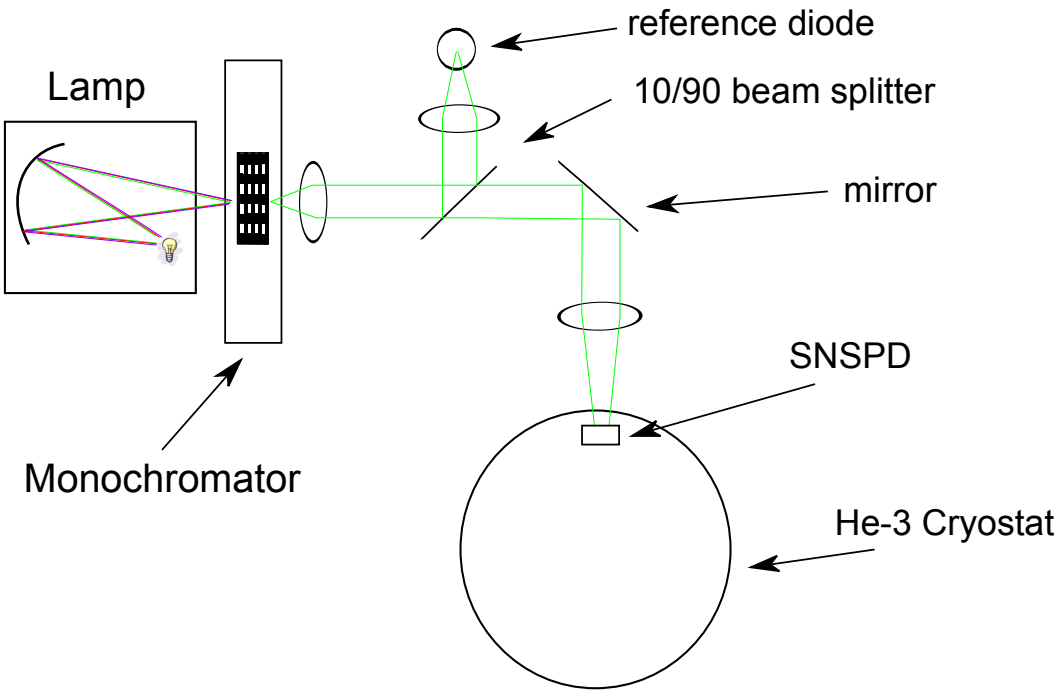

Figure 11: Schematic sketch of the optical setup. After leaving the monochromator the light reaches the beam splitter. There it is partially reflected and focused on a diode as a reference. The larger part of the lights intensity is transmitted and guided into the cryostat and onto the SNSPD. The lens between the beam splitter and the cryostat is placed in a way that the SNSPD is a little bit out of focus to ensure a homogeneous illumination.

Material	Width [nm]	Height [nm]	No of Lines	Area [μm $\times$ μm]	Fill Factor
NbN	80	5	25	5 $\times$ 4.92	0.4
TaN	126	3.9	21	3.4 $\times$ 4.2	0.63

Table 1: Most important geometric dimensions of the two SNSPDs.

5 Device Characterization

5.1 Structures

The SNSPDs we used are made from thin films grown on sapphire substrates by DC magnetron sputtering. Sapphire has a very high thermal conductivity and a high transmission for light from infrared to ultraviolet, which leaves the possibility to expose the nanowire to light from the back side of the chip. It is also well suited for the fabrication process because it has a small lattice mismatch to NbN and TaN, and it is chemically stable. Also sapphire acts as an etch-stopper what makes the chip more resistant to possible variations of etch-time and etch-rate. The films need to be very pure and since the facility available to us is not satisfactory, the films were made by our collaborators at the Institute of Micro- and Nano-Electronic Systems at the Karlsruhe Institute of Technology. Then the films are structured by e-beam lithography to a nanowire in a meander shape in order to cover an area as large as possible. The NbN-meander was structured at the FIRST Laboratory, a clean room at ETH Zurich, the TaN-meander was entirely fabricated at the University of Karlsruhe. For a detailed description of the fabrication process please refer to [24].

The important geometric properties were determined by the analysis of SEM-pictures and are listed in table 1. The fill factor indicates how much of the detector-area is covered by the nanowire.

5.2 Device Properties

The superconducting properties of the nanowires relevant for this study have been derived from resistivity measurements in a commercial Physical Property Measurement System (PPMS). The resistances have been measured from 300 K to 3 K with the samples exposed to magnetic inductions from 0 Tesla to 9 Tesla. From these data the values in table 2 have been calculated using the relations in section 2.1 and geometric dimensions from table 1. In figure 12, a resistance measurement of the NbN-SNSPD is shown. The transition temperature was determined by the $\frac{R_n}{2}$-criterion. When measuring the resistance from room temperature to lower temperatures in the normal conducting phase an increase of resistance can be observed. This is either due to "weak localization" [25] or "grain-boundary scattering" [26]. For the normal state resistance R_n, the maximal value

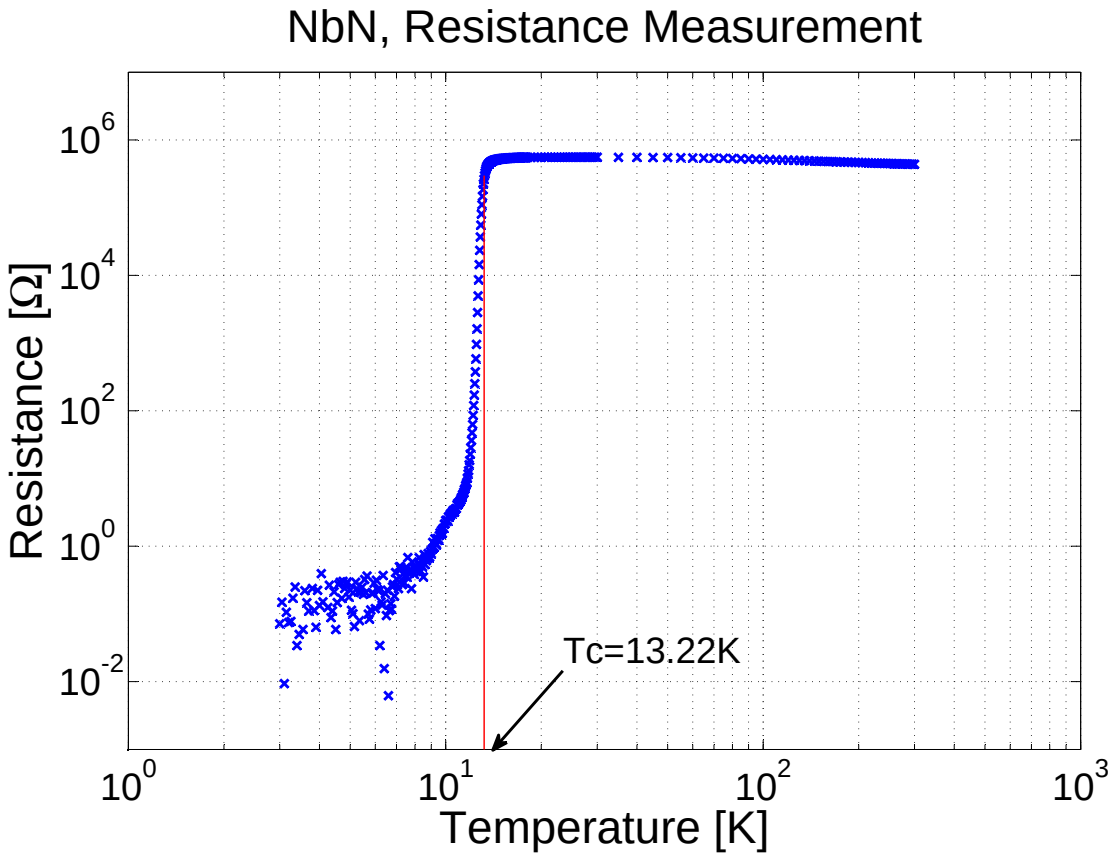

Figure 12: Resistance measurement performed in a PPMS with no magnetic field applied. The phase transition occurs at 13.22 K. R_n is taken as the maximum of the resistance curve.

of the resistance curve was taken, close to the transition temperature. The resistivity in the normal conducting state, ρ_n, is given by the geometry and R_n using Eq.(6).

The diffusion coefficient D was calculated according to Eq.(4). The differential factor in Eq.(4) was determined by fitting a linear function to the data obtained by the resistance measurements in a magnetic field. The same factor was used to calculate the upper critical field using Eq.(11). $B_{c2}(0)$ is used by applying Eq.(12) to calculate $\xi(0)$. The density of states at the Fermi-level ($DOS(E_F)$) is calculated using Eq.(5). The energy gap Δ for the strongly coupled NbN-film can be determined by Eq.(8). Due to lack of better knowledge the energy gap for the TaN-film was calculated using the BCS-relation Eq.(7). The magnetic penetration depths λ and Λ are given by Eq.(15) and Eq.(18) respectively. Those parameters are regarded as constant since the experimental temperatures are always below $\frac{T_c}{2}$. The theoretical value for the critical depairing current $I_{c,d}$

Material	$\mathbf{R_n}$ [Ω]	ρ_n [Ωm]	$\mathbf{T_c(R_n/2)}$ [K]	D [$\frac{m^2}{s}$]	$\mathbf{DOS(E_F)}$ [$m^{-3}J^{-1}$]	$\mathbf{\Delta(0)}$ [meV]
NbN	$5.56 \cdot 10^5$	$1.74 \cdot 10^{-6}$	13.22	$5.25 \cdot 10^{-5}$	$4.27 \cdot 10^{47}$	2.4
TaN	$3.33 \cdot 10^5$	$2.28 \cdot 10^{-6}$	8.34	$6.06 \cdot 10^{-5}$	$2.82 \cdot 10^{47}$	1.5

Material	$\lambda(0)$ [nm]	$\Lambda(0)$ μm	$\mathbf{B_{c2}(0)}$ [T]	$\frac{dBc2(T)}{dT}$ [$\frac{T}{K}$]	$\xi(0)$ [nm]	$\mathbf{I_{c,d}(0)}$ [μA]
NbN	349.7	48.9	19.536	-2.09	4.1	76.72
TaN	504.4	129.5	10.667	-1.81	5.55	22.63

Table 2: Most important superconducting properties of the two SNSPDs. The properties and their calculation are mentioned in the text.

was calculated from Eq.(19).

5.3 Light Source Calibration

In order to know how many photons are incident on the SNSPD for a given wavelength, the light source had to be calibrated. By measuring the count rate dependence on bias current or photon wavelength, the calibration values allow to calculate a quantum efficiency. To calibrate the light source, a calibrated diode was placed where the SNSPD would be mounted later. The heat shields on the cryostat were demounted on one side but not on the side facing the light beam. Only the not-splittable vacuum cover had to be removed entirely. The missing quartz glass window was replaced by a free standing quartz glass that was mounted on the optical board. Two calibrated diodes manufactured by Thorlabs were used. A Si-diode for wavelengths between 200 nm and 1000 nm and a Ge-diode for wavelengths between 1000 nm and 1700 nm. The diodes were connected to a controller box that provides the user directly with the calibrated power values incident on the diode. The controller box can be connected to a PC and controlled by a Labview software. The diodes were partially covered by a circular aperture with a diameter of 0.424 mm. For the calibration of the spectrum between 200 nm and 1000 nm a Si pin-diode was placed as a reference (see figure 4). The spectrum was scanned with the monochromator and the current signal of the reference diode was read out by a Keithley 6487 Picoammeter that was connected to a PC. While scanning through the spectrum, the current values from the reference pin-diode and the power values from the calibrated Si-diode were recorded at the same time. For the IR spectrum from 1000 nm to 1700 nm the calibrated Ge-diode was used at the place of the SNSPD and as the reference as well. A first attempt to use a PbSe-diode as a reference had to be dismissed because the diode showed a non linear response to different light intensities. The spectrum was scanned twice, once with the Ge-diode at the place of the SNSPD, and once in the reference site. With those values, a calibration table was calculated. The

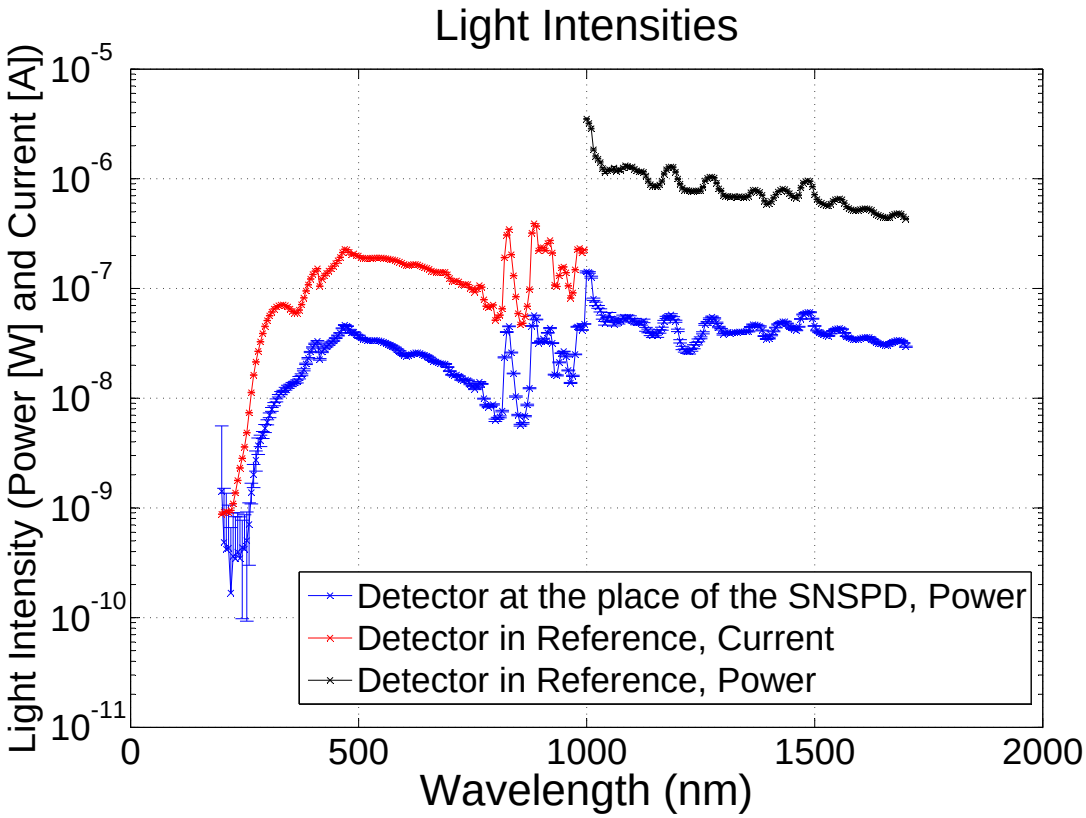

Figure 13: Light intensity measurements used for the calibration of the light source. The blue curve represents the power measured at the place of the SNSPD. The red curve is the current measured by the Si reference-diode and the black curve is a measurement of the power, both in the reference site.

light intensity was only practical for wavelengths above 300 nm, and the use of the Ge-diode restricted the calibration values available for wavelengths up to 1700 nm. Figure 13 shows measurements of the spectrum of the lamp at the place of the SNSPD and the reference site. The light intensity changes over two orders of magnitude over the entire spectrum. The reference diodes are also in place during the photon-count measurements to account for changes in the light intensity of the lamp, assuming a linear response.

5.4 Quantum-Efficiency Measurements

To learn more about SNSPDs based on TaN and to compare the detection properties to SNSPDs made of NbN, count rates of the NbN- and TaN-SNSPD have been measured at different conditions. The count rate has been measured as a function of both the photon wavelength and the bias current. From the obtained values the quantum efficiency was

calculated using the calibration table (see section 5.3). All measurements have been conducted at several temperatures.

According to Eq.(27) the SNSPD has to be biased with a current close to I_c in order to detect photons with low energy. If a photon is absorbed in the meander structure or a fluctuation occurs, a resistive domain is formed. For a fast photon-count it is very important that the excited states responsible for the formation of the resistive domain relax back as fast as possible. As mentioned in section 5.1 the sapphire substrate has a good thermal conductivity, which is essential for the fast relaxation of the SNSPD.

If the SNSPD is biased with a constant bias current close to the critical current, electronic noise or sudden fluctuations can switch the nanowire partially into the normal conducting state. If so, the phase transition leads to a finite resistance that causes Joule heating. The heat produced hampers the device to switch back into the superconducting state, and the increased voltage can possibly harm the nanowire. To avoid this problem, a constant voltage drives the current. The current is constant as long as the nanowire is in the superconducting state. If the superconducting state is disturbed by electronic noise, and part of the nanowire switches into the normal-conducting state without switching back to the superconducting state the current is reduced substantially, allowing the system to relax when the voltage is reduced, and preventing the device from damage.

If the bias current passes over the experimental critical-current $I_{c,exp}$, part of the nanowire switches into the normal conducting state. Tiny constrictions and inhomogeneities in the conduction path make some lines of the meander more vulnerable to the bias current than others. The critical current mentioned in section 2 is a theoretical value as it can be derived from Ginzburg-Landau Theory. The experimental critical-currents derived from I-V characteristic in the following sections deviate from theory. If a bias current close to the theoretical critical-current $I_{c,GL}$ can be reached, it is a sign of good homogeneity of the conduction path. The experimental critical-current $I_{c,exp}$ that are presented in the following have been determined by I-V-characteristics conducted in the optical cryostat using the same current source and the same operation temperatures as in the photon counting measurements. Figure 14 shows an I-V-characteristic for the TaN-SNSPD at 610 mK in constant voltage mode. The current rises with increased voltage linearly because of a constant resistance of the cables. If the current reaches the critical current, the superconducting state is destroyed and the resistance rises substantially. Since the voltage is kept constant, the current reduces. If the voltage is reduced the superconducting state is not recovered at once. The voltage has to fall below a certain "return voltage" for the superconducting state to reappear.

In the following the experimental critical-current will be denoted $I_{c,exp}$ or I_c and the theoretical critical-current $I_{c,GL}$.

Of particular interest is the cutoff condition mentioned in section 3.1, Eq.(27), that separates the two detection regimes ("direct detection" (see section 3.1) and "detection via fluctuation" (see section 3.1.1)). For a fixed bias-current a cutoff wavelength corresponding to a cutoff energy can be defined, and at fixed wavelength one can define a

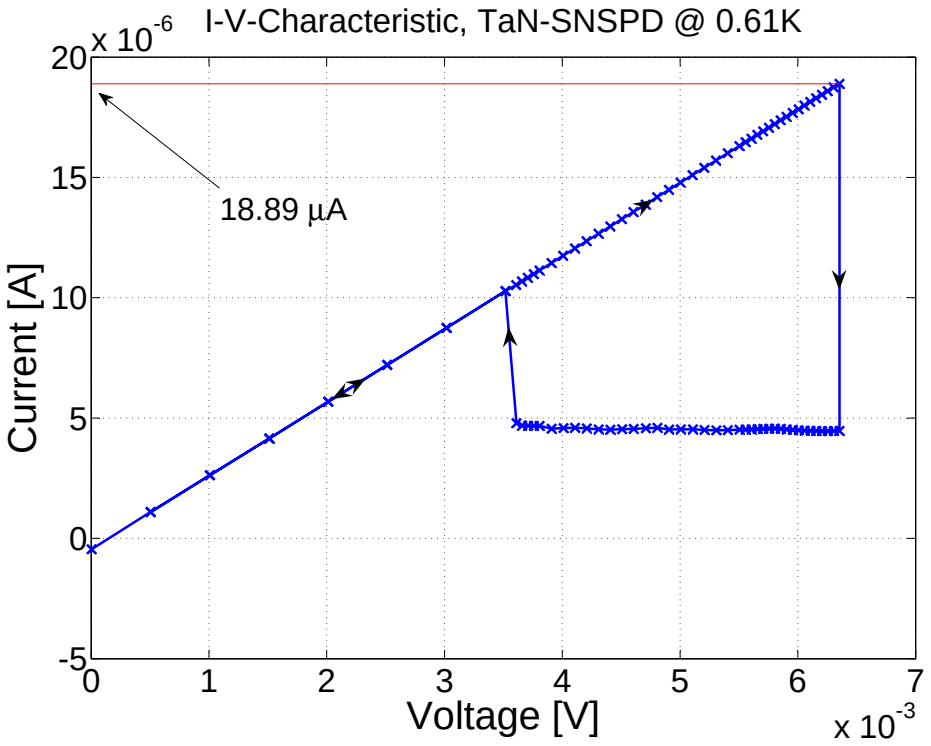

Figure 14: I-V-characteristic for the TaN-SNSPD at 610 mK in constant voltage mode. The current rises with increased voltage linearly because of a constant resistance of the cables. If the current reaches the critical current, the superconducting state is destroyed and the resistance rises substantially. Since the voltage is kept constant the current reduces. If the voltage is reduced the superconducting state is not recovered at once. The voltage has to fall below a certain "return voltage" for the superconducting state to reappear. The critical current is indicated. See also table 6 for the critical currents of the TaN device and table 3 for the critical currents of the NbN device.

T [K]	$\mathbf{I_{c,exp}}[\mu\mathbf{A}]$	$\mathbf{I_{c,GL}}[\mu\mathbf{A}]$	% of $\mathbf{I_{c,GL}}$ reached
0.5	35.19	76.61	46%
1.9	35.39	75.12	47%
5	29.49	65.08	45%

Table 3: Theoretical and experimental critical-currents of the NbN nanowire at the temperatures of the photon-count measurements. The theoretical critical-current $I_{c,GL}$, is calculated using (19). The experimental critical-current $I_{c,exp}$ has been determined by I-V-characteristics.

cutoff bias-current with the same physical meaning.

If the cutoff conditions are satisfied ($\lambda < \lambda_{cutoff}$, $I_b > I_{b,cutoff}$) the limiting factors for the quantum efficiency of the wavelength investigated are the filling factor, the photon absorbability in the nanowire, and constrictions of the conduction path. In the case of satisfied cutoff conditions the quantum efficiency as a function of the bias current and the photon wavelength should be a horizontal line, only dependent on the absorbability. In the following the measurements of quantum efficiency are presented, and if possible, a cutoff condition has been determined.

5.4.1 NbN

The quantum-efficiency measurements of the NbN-SNSPD were conducted at three temperatures. For each temperature the critical current has been determined from I-V measurements. The results are shown in table 3.

Bias-Current Scan The quantum efficiency as a function of the bias current has been measured for four wavelengths at each temperature. A fifth bias-current scan with the light source switched off was done to measure the background signal of the SNSPD. This background signal consists on the one hand of the background photons from inside and outside the cryostat (lab illumination, reflected sunlight, blackbody radiation), on the other hand there are intrinsic fluctuations of the SNSPD, so-called dark counts. The background measurements are subtracted from the measurements at constant wavelength to get a count rate that only stems from the photons from the lamp. The scans were performed up to a bias current as close to the experimental critical-current as possible. Close to $I_{c,exp}$ the SNSPD is very sensitive to electronic noise and keeps switching partially into the normal conducting state. Because of that the bias scans were only performed to a bias current slightly above 90% of the experimental critical-current. The bias scans are shown in figures 15 to 17. When scanning the bias current, at each setting the mean value of five single measurements over one second was taken as the count rate and the standard deviation of those measurements was regarded as the error of the count rate. A flat plateau, as expected from theoretical considerations at high bias currents,

Temperature [K]	Wavelength [nm]	Cutoff Bias-Current [% I_c]
0.5	300	62.1
1.9	300	67
5	300	75.4

Table 4: Summary of the cutoff condition of the NbN-SNSPD resulting from bias-current scans at fixed wavelength.

cannot be clearly observed. Instead, in the scans at 300 nm the curve shows a steady increase at high bias currents. This increase most likely stems from inhomogeneities in the conduction path. If the nanowire varies in width, at a certain bias current some narrow sections are already in saturation but for wider sections the bias current has to be increased to reach saturation. The relatively low experimental critical-current compared to the theoretical critical-current (see table 3) supports this assumption.

The cutoff bias current for the bias scans at 300 nm were determined by the intersection of two exponential fits, one fitting the steep rise of the quantum efficiency at lower bias currents and another one fitting the saturation. The results are shown in table 4. The interpretation of the bias scans performed at 600 nm and 800 nm for 0.5 K and 1.9 K and at 600 nm for 5 K is not so clear. The change of the slope is not as pronounced as for the scans performed at 300 nm, but still the quantum efficiency reached a relatively high value. It can be suspected that these measurements could show a plateau-like behavior at higher bias currents. Unfortunately, this region of bias currents above 90% was not accessible. By linearly extrapolating these curves, the quantum efficiencies reach the value of the 300 nm curve or even above. Therefore, it is assumed that these curves reach saturation, but a definitive cutoff bias-current cannot be determined. The scans performed at 1100 nm for 0.5 K and 1.9 K as well as at 1100 nm and 800 nm for 5 K are very unlikely to reach saturation at any point and it is reasonable to assume that those wavelengths lie above the cutoff wavelength for all measured bias currents at the given temperature.

Unexpectedly the measurements show a temperature dependence of the cutoff conditions that is not predicted by Eq.(27). The temperature does have an influence on the size of the energy gap, but because the energy gap gets smaller with increased temperature the cutoff would occur at lower energies or lower bias-currents. The measurements yield the opposite situation.

Wavelength Scan For each of the three temperatures four bias currents were chosen to perform the wavelength scans. In order to only count the photons coming from the lamp at each wavelength the background count was measured and subtracted from the count rate. The wavelengths were scanned from 220 nm to 1700 nm. The results of the scans are shown in figures 18 to 21. At each wavelength the count rate was averaged over

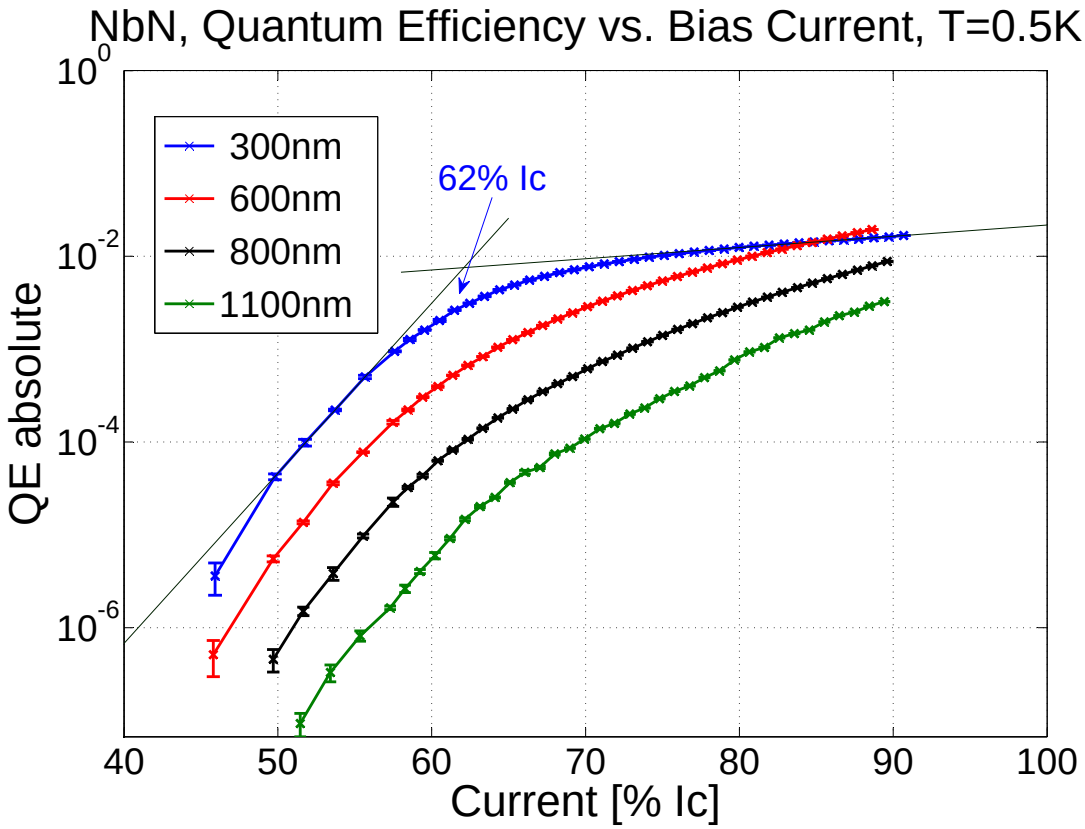

Figure 15: Quantum efficiencies as a function of the reduced bias current of the NbN-SNSPD at 500 mK. The bias current was scanned at four fixed photon wavelengths. The cutoff current was determined by the intersection of the two fits and is indicated by the arrow.

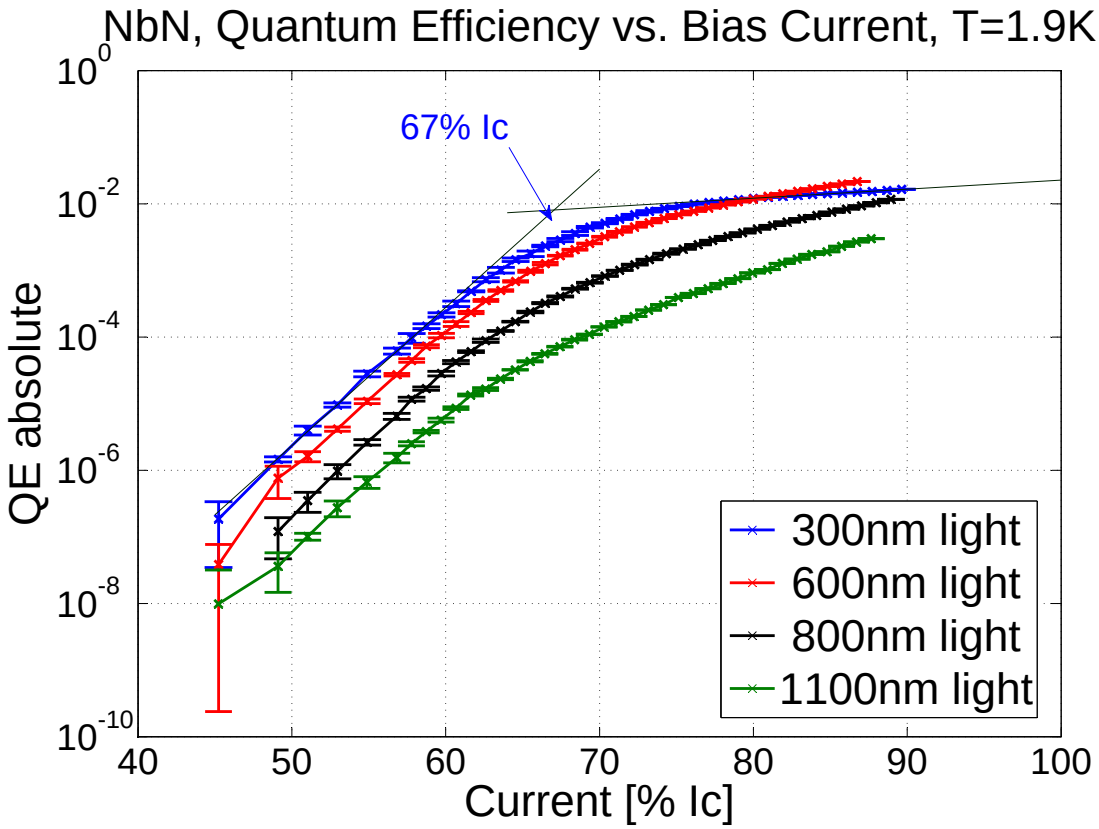

Figure 16: Quantum efficiencies as a function of the reduced bias current of the NbN-SNSPD at 1.9 K for four photon wavelengths. The cutoff current (intersection of the fit-lines) is indicated by the arrow.

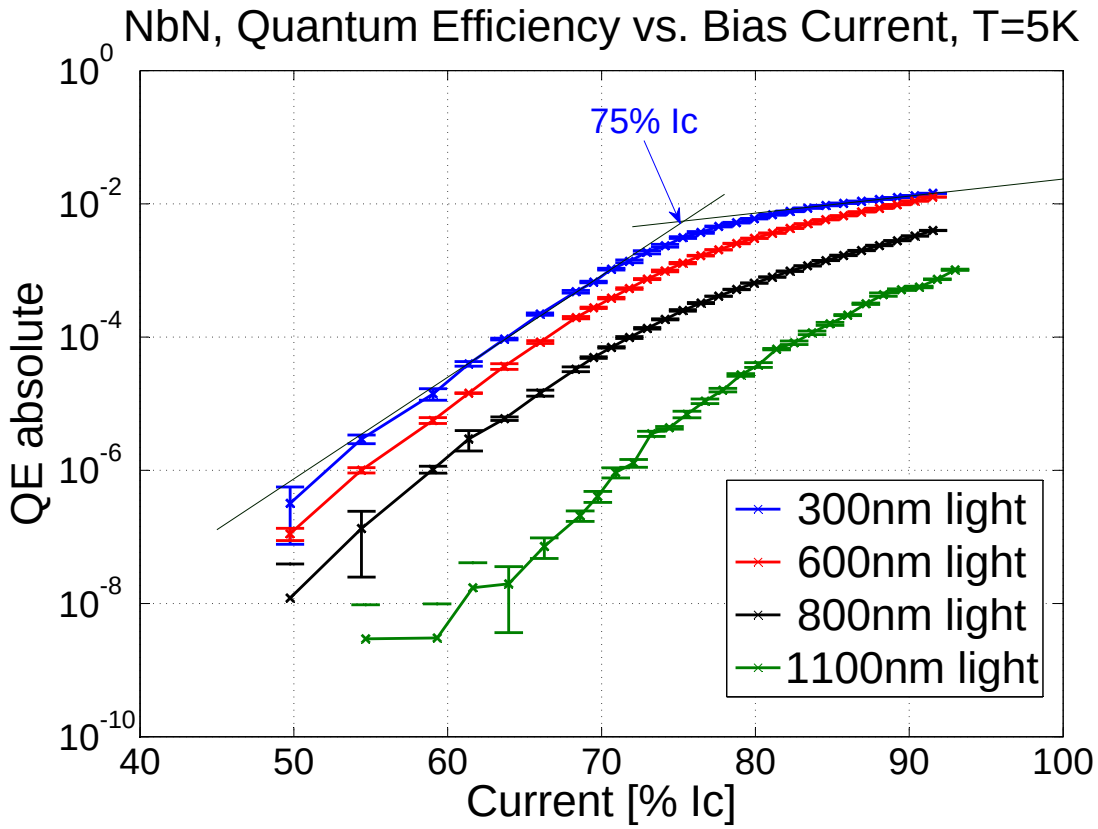

Figure 17: Quantum-efficiencies as a function of the reduced bias current of the NbN-SNSPD at 5 K for four photon wavelengths. The cutoff current (intersection of the fit-lines) is indicated by the arrow.

five single measurements and its error is the standard deviation of those measurements. Compared with the bias-current scans, the value for the quantum efficiency measured by scanning the wavelength is about an order of magnitude higher. This might be explained by the fact that the current-scans and the wavelength-scans were performed about six month apart. During this period, the optical setup was taken apart and reassembled, the light bulb of the lamp was replaced, and a new set of calibration factors was determined.

As mentioned in section 5.3, the light intensity below 300 nm is very weak compared to the sensitivity of the semiconductor detectors used for the light source calibration, which resulted in very high statistical errors. Because of that, a flat plateau as expected from theoretical considerations cannot be observed. Considering the bias scans mentioned in the paragraph above, the bias scans performed at 300 nm wavelength reached saturation at some point. Since the wavelength scans with the highest bias current are performed above 90% of the critical current, it is assumed that their cutoff wavelength must be above 300 nm and the cutoff is hidden in the systematic errors of the curve. Looking closely at the wavelength scans from say 260 nm to 400 nm, one can see that the slope of the quantum efficiency of the scans at 0.5 K and 1.9 K start out as the same, but at some point, they drift apart. It is reasonable to assume that in the region where the characteristics are parallel, the detector is saturated and the decrease of the quantum efficiency is due to systematic errors. With that in mind, a set of conversion factors has been calculated that move the reference curve (the curve with the highest bias current) on top of the curve to be analyzed. In the region of parallel characteristics the conversion factors will be the same, but when the curves start to drift apart those factors decrease, indicating the cutoff wavelength. Figure 19 shows that exemplarily for an analysis of the results obtained at 0.5 K and a bias current of 88.9% I_c. Still, the interpretation is not clear. The first few factors are constant, but after 320 nm the factors start to decrease weakly. A pronounced decrease of the factors sets in after 380 nm. This was regarded as the cutoff wavelength.

In this manner the cutoff wavelength of the NbN-SNSPD were determined for 0.5 K and 1.9 K and the results are summarized in table 5. For the scans performed at 5 K the curves start to drift apart already at very small wavelengths where the statistical errors are quite large. For those measurements no cutoff conditions could be determined.

5.4.2 TaN

The quantum-efficiency measurements of the TaN-SNSPD were also conducted at three temperatures. For each temperature the experimental critical-current has been determined from I-V measurements. The results are shown in table 6.

Bias-Current Scan The quantum efficiency depending on the bias current has been measured for several wavelengths at each temperature. The procedure to obtain a value for the count rate was analog to the bias-current scans of the NbN-SNSPD. The

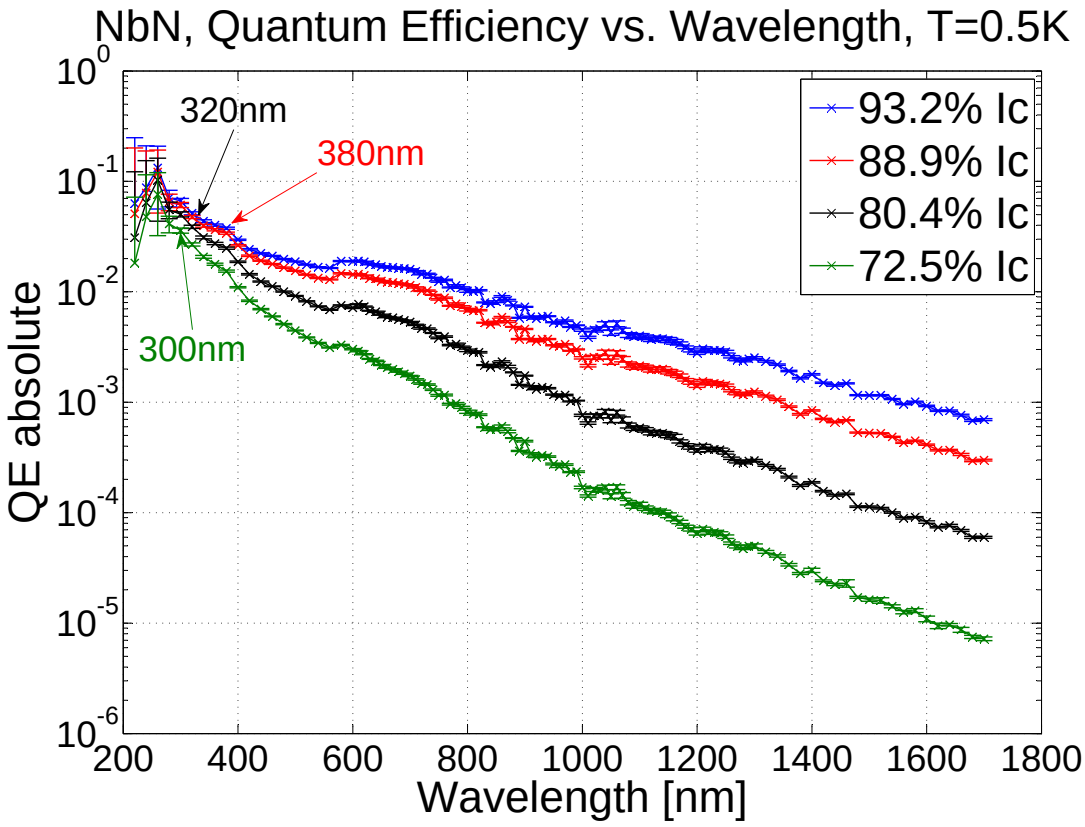

Figure 18: Quantum efficiencies of the NbN-SNSPD at 500 mK at four fixed bias currents. The cutoff wavelength as determined by the method described in the text is indicated by arrows.

Temperature [K]	Bias Current [% I_c]	Cutoff Wavelength [nm]
0.5	88.9	380
0.5	80.4	320
0.5	72.5	300
1.9	89	320
1.9	80.2	320
1.9	72.1	300

Table 5: Summary of the cutoff conditions of the NbN-SNSPD resulting from wavelength scans at fixed bias current.

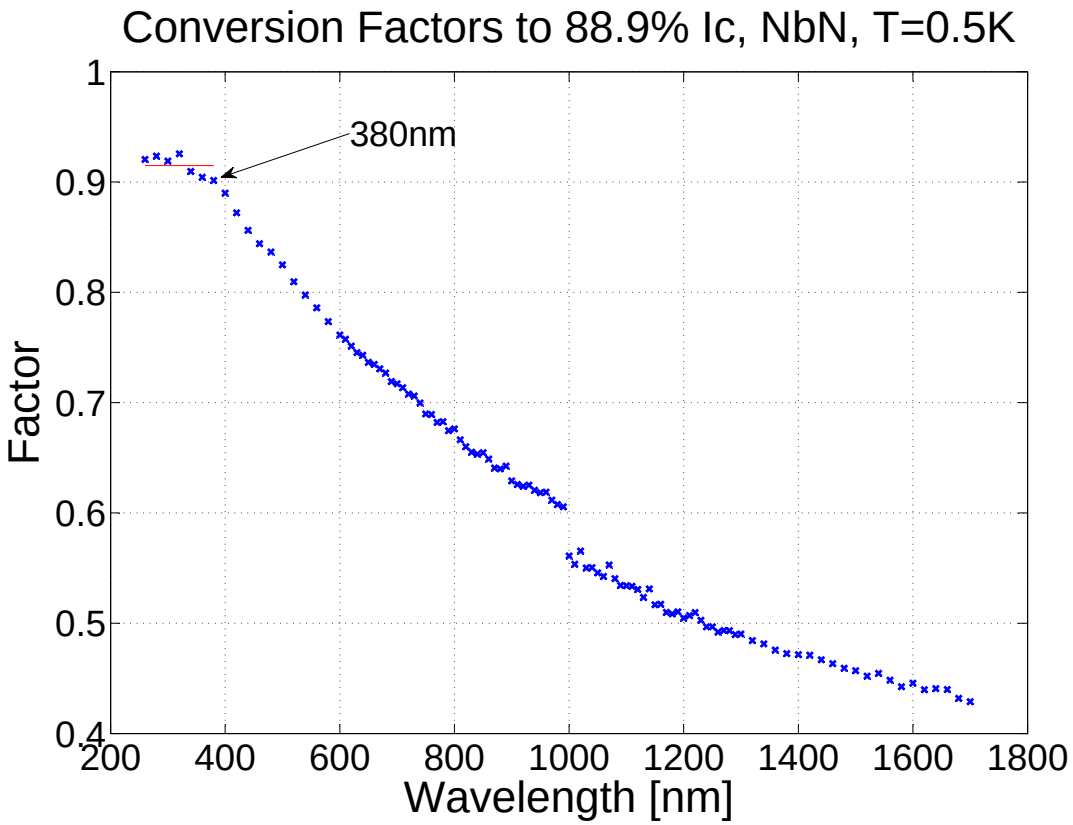

Figure 19: Example for the conversion factors used to determine the cutoff wavelength of the quantum-efficiency measurements dependent on wavelength of the NbN-SNSPD. The set shown is used to scale the measurement at 93.2% I_c onto the measurement at 88.9% I_c, both at 500 mK. The turnover from constant factors to the decrease defines the cutoff wavelength. Such a set of conversion factors was used for each bias current and each temperature to determine the cutoff wavelength.

T [K]	$\mathbf{I_{c,exp}}[\mu\mathbf{A}]$	$\mathbf{I_{c,GL}}[\mu\mathbf{A}]$	**% of $\mathbf{I_{c,GL}}$ reached**
0.61	18.89	22.51	83.93
2	17.89	21.29	84.03
4	13.96	16.96	82.33

Table 6: Theoretical and experimental critical-currents of the TaN nanowire at the temperatures of the photon-count measurements. The theoretical critical-current $I_{c,GL}$, is calculated using (19). The experimental critical-current $I_{c,exp}$ has been determined by I-V-characteristics.

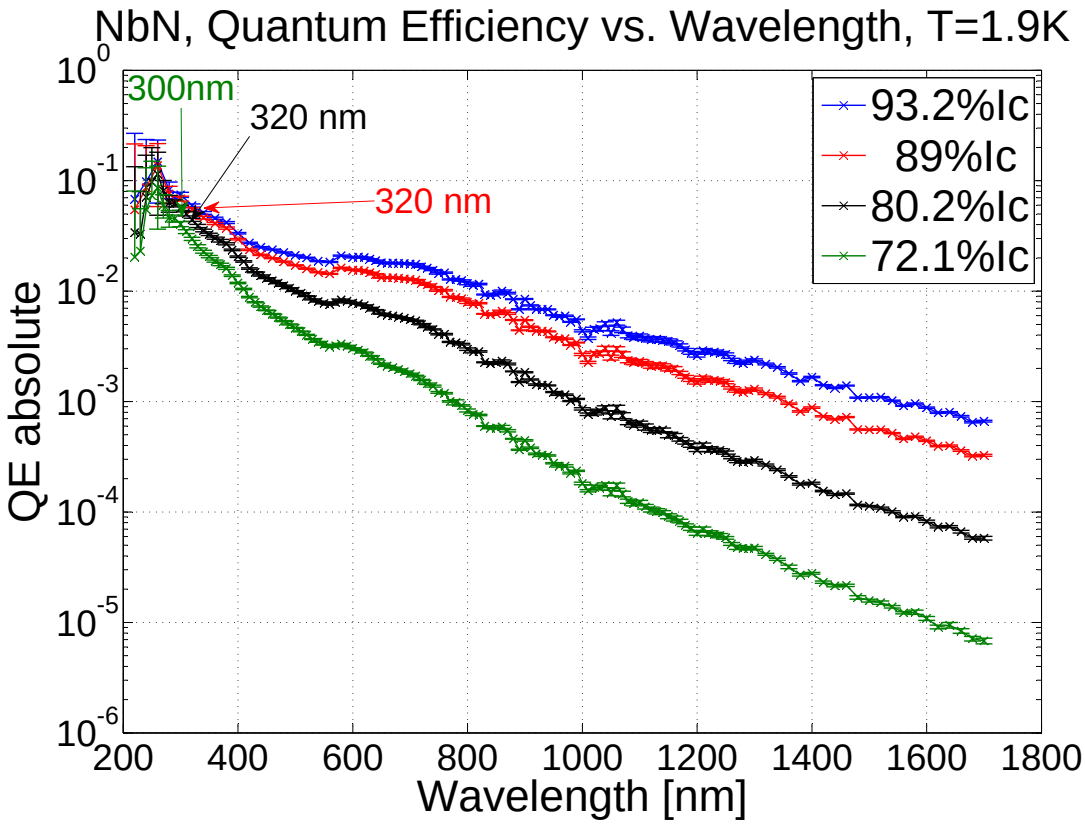

Figure 20: Quantum-efficiency measurements of the NbN-SNSPD at 1.9 K at four fixed bias currents. The cutoff wavelength is indicated by arrows.

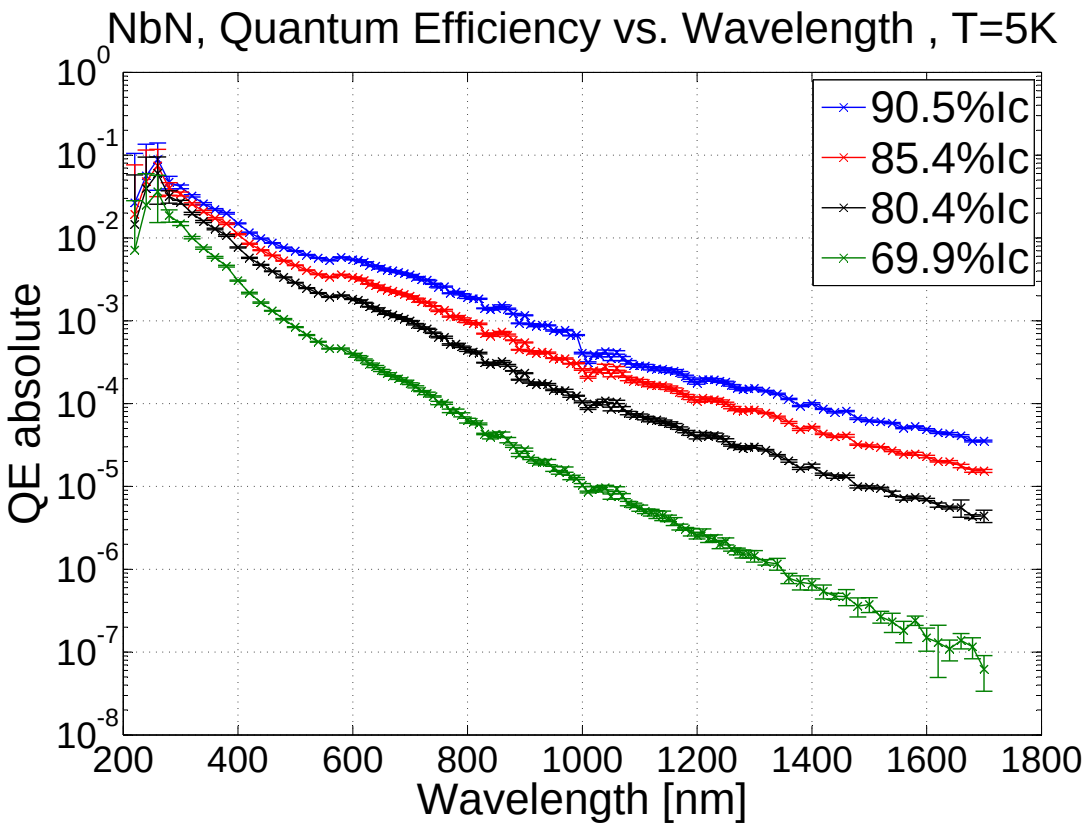

Figure 21: Quantum-efficiency measurements of the NbN-SNSPD at 5 K at four fixed bias currents. For the measurements at 5 K no cutoff wavelength could be determined within the spectrum available.

background photons and intrinsic fluctuations were measured and subtracted from the count-rate measurements. At each setting the count rate was averaged over five single measurements and the standard deviation of those single measurements were regarded as the error of the count rate. The bias current was raised to a value as close as possible to the experimental critical-current. Since either the system is not as sensitive to electronic noise as the NbN-SNSPD, or there was less electronic noise, the bias current could reach over 98% of the experimental critical-current. The measurements are shown in figures 22 to 24. Looking at figures 22 and 23 for the scans at 300 nm, an almost flat plateau can be observed. This is an indication of a quite homogeneous conduction path unlike the NbN-SNSPD (see section 5.4.1). Further support for this assumption comes from the experimental critical current that is much closer to the theoretical critical current compared to the NbN system (see table 6), but this could also be the result of more stable operation conditions. In the measurements at 0.61 K and 2 K saturation has clearly set in and the cutoff bias currents were determined by intersecting the fits of the two major characteristics of the curves. The quantum-efficiency value that the curves yield at the cutoff bias current in reference with the quantum-efficiency value at saturation give a reduction factor. These reduction factors are very close to 52% for the measurements at 0.61 K and 2 K. Assuming this is the same for all the wavelengths, it allows the calculation of the cutoff bias currents of the measurements for higher wavelengths.

The interpretation of the measurement at 4 K proves to be more difficult. No pronounced plateau can be observed, contrariwise, the curves show new characteristics, very pronounced at 300 nm to 800 nm and less pronounced at 900 nm to 1100 nm. A closer look at the pulse shape yields a possible explanation in the case of 300 nm. The amplitude of the pulses rise with increased bias current and eventually become large enough that the second and possibly also the third peak can trigger a counting event since the discriminator level was fixed for the scans. Indeed, if the "lower plateau" is extrapolated to higher bias currents (like in the fit-line in figure 24) the value of the quantum efficiency is 2.63 times lower than in the measurement, supporting the hypothesis of multiple counts per event. With that in mind, the "lower plateau" was used for the fit to determine the cutoff bias current. The shape of the curves for high bias currents at 600 nm to 1100 nm are anomalies that cannot be explained at the present time. The cutoff for the measurement at 600 nm was determined as described above. Here, the reduction factor was calculated as 15% what differs strongly from the ones at 0.61 K and 2 K. That can be regarded as an indicator that the results obtained at 4 K have to be treated with care. For the measurements at higher wavelengths the change of the slope of the overall curves is not pronounced enough, so it is assumed that they are showing no cutoff. The results are summarized in table 7. Similar to the results of the bias-current scans of the NbN-SNSPD the cutoff bias-current shows a unexpected temperature dependence.

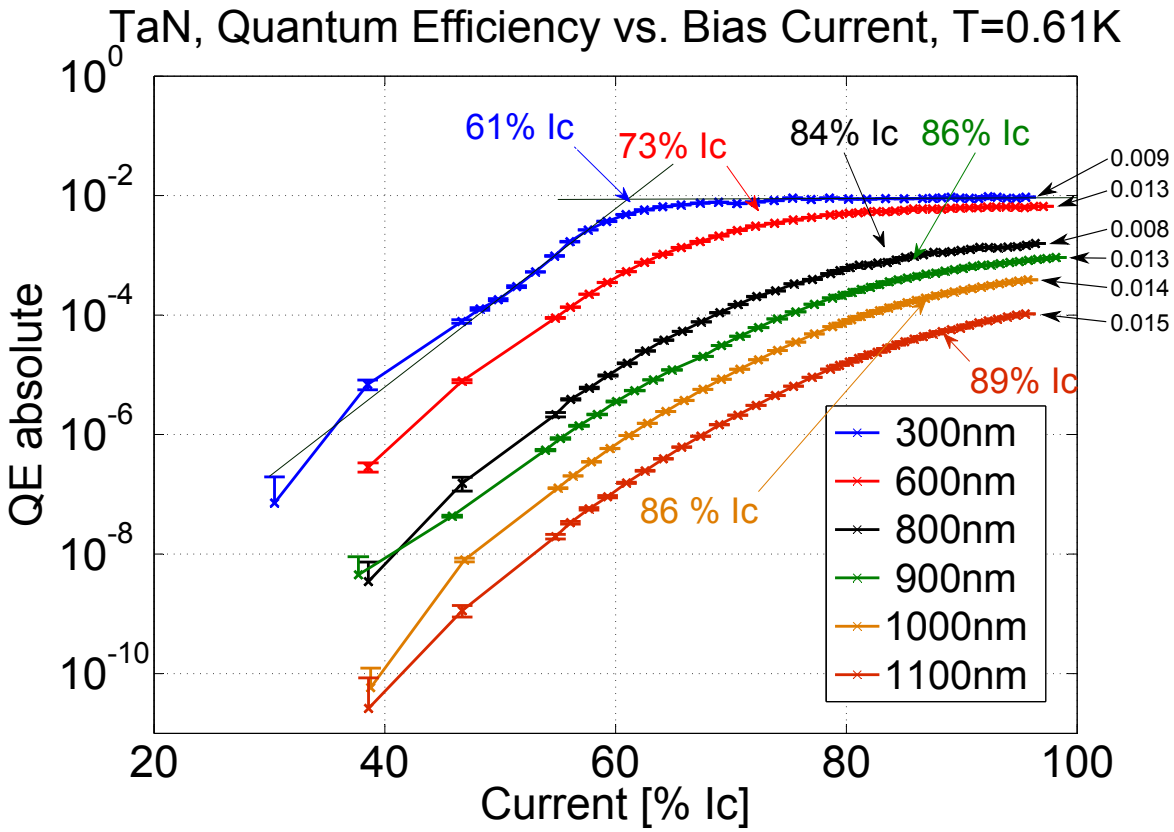

Figure 22: Quantum efficiencies as a function of bias current of the TaN-SNSPD at 610 mK. The bias current was scanned at six fixed photon wavelength. Except for the 300 nm curve, all the curves have been shifted for clarity. The true values for the last data points are indicated. The cutoff current of the measurements at 300 nm was determined by the intersection of the horizontal line and an exponential function. The fit lines are indicated. The cutoff currents of the other measurements were determined by the reduction factor of the 300 nm curve (see main text for more details).

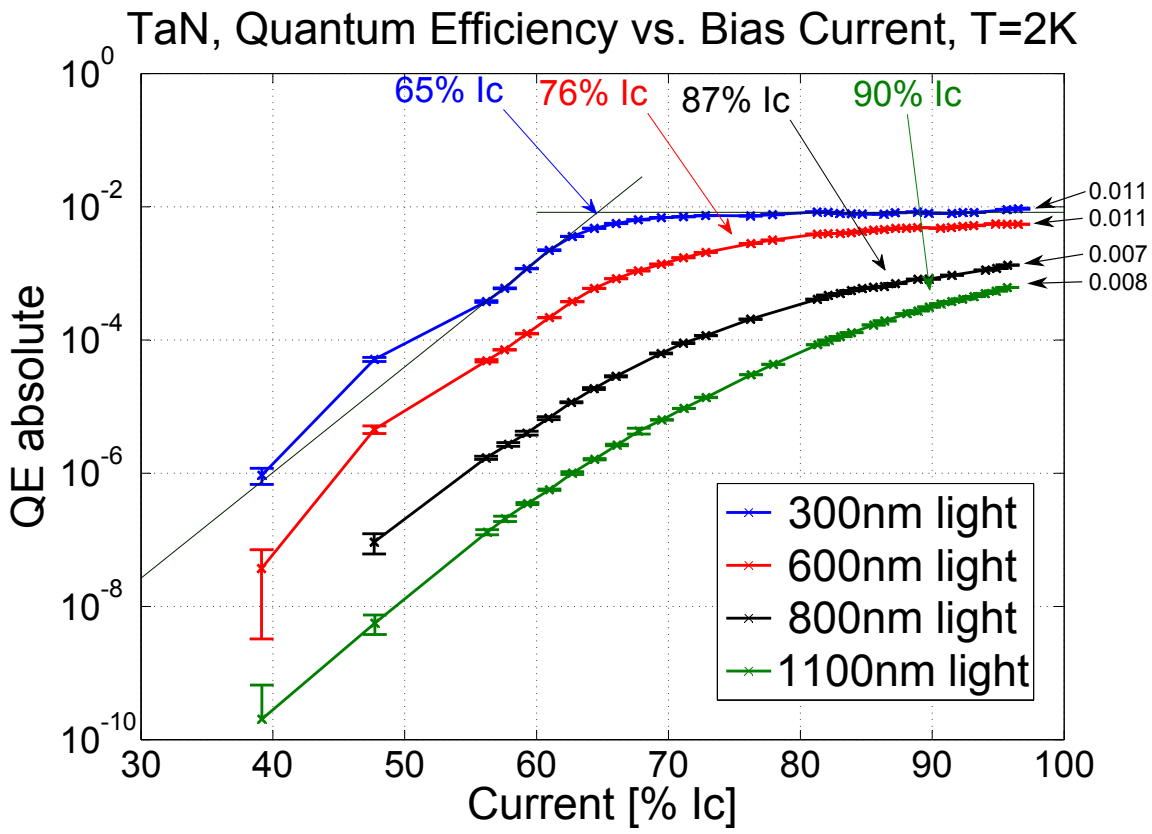

Figure 23: Quantum efficiencies as a function of bias current of the TaN-SNSPD at 2 K. (See caption of figure 22.)

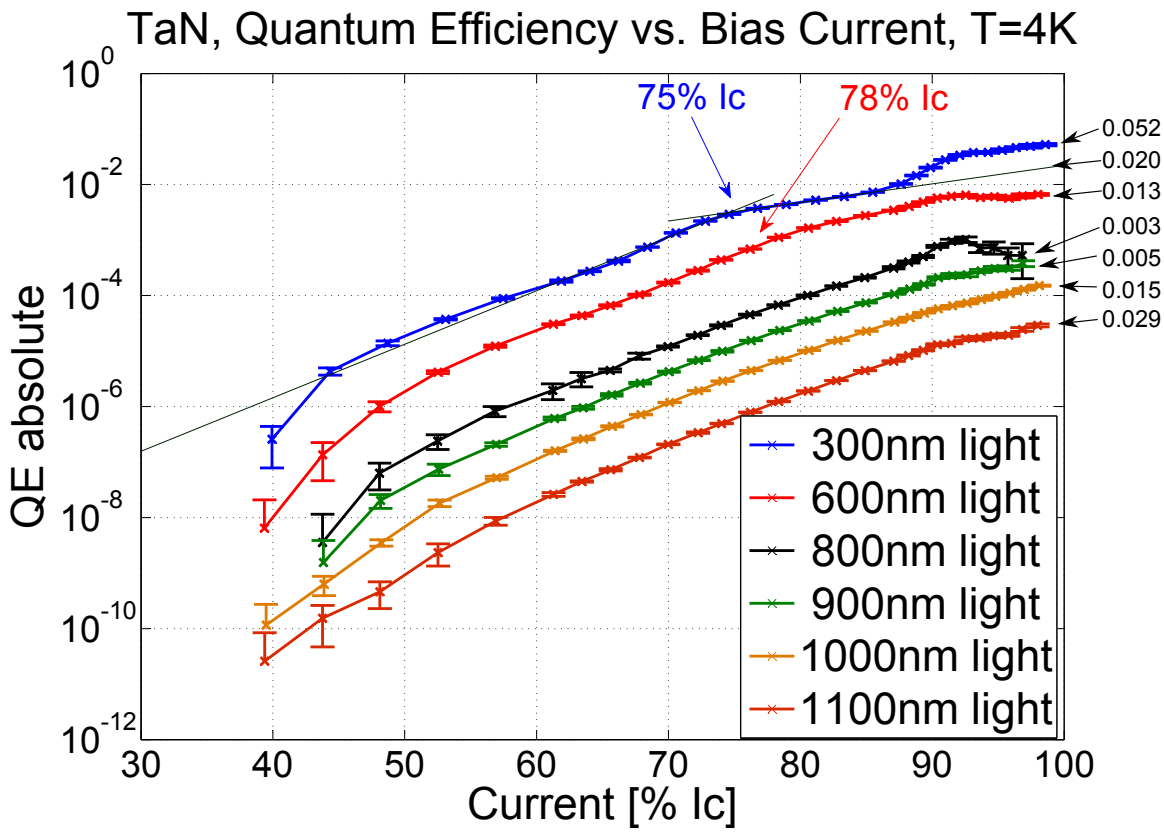

Figure 24: Quantum efficiencies as a function of bias current of the TaN-SNSPD at 4 K. See caption of figure 22.

Temperature [K]	Wavelength [nm]	Cutoff Bias-Current [% I_c]
0.61	300	61.1
0.61	600	73.8
0.61	800	84.2
0.61	900	86.8
0.61	1000	87.4
0.61	1100	88.7
2	300	64.5
2	600	76.3
2	800	87
2	1100	89.9
4	300	74.7
4	600	77.5

Table 7: Summary of the cutoff condition of the TaN-SNSPD resulting from bias-current scans at fixed wavelength.

Wavelength Scan The quantum efficiencies as a function of photon wavelength have also been measured for the TaN-SNSPD at three temperatures. The wavelengths were scanned from 300 nm to 1700 nm, and in analogy to the measurements of the NbN-SNSPD the background was measured at every wavelength and subtracted from the count rate. The determination of the count rate and the errors were also done in the same way. Figure 25 shows measurements performed at 0.61 K with four bias currents. The data looks very messy and no plateau can be observed. However, looking closely at the upper three curves, all the pronounced features appear to be the same. This brings up the suspicion that those features stem from systematic errors of the calibration. Assuming that is the case, the weighted mean of the values between 800 nm and 1040 nm of the 91.6% I_c-curve at 0.61 K have been calculated and a set of coefficients has been deduced that scale the results to the value of the weighted mean. This interval was chosen, because it contains the most pronounced systematic errors and from table 7 the cutoff wavelength is expected to be larger than 1100 nm for this measurement. Applying the same set of coefficients to all the other measurements the curves could be smoothened and a plateau or a exponential-like decrease can be observed. The smoothened measurements are shown in the figures 26 to 28.

Also here, the intersection of the fits of the flat plateau and the exponential-like decrease determine the cutoff wavelength. The results are shown in table 8.

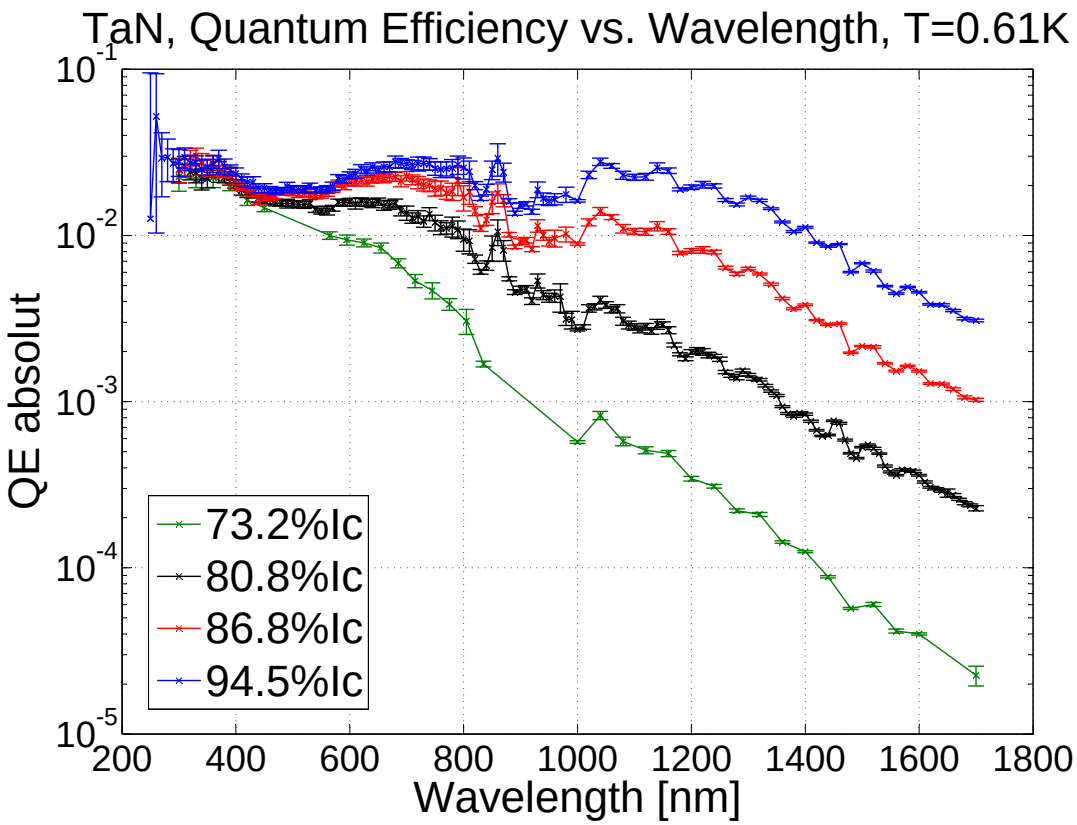

Figure 25: Unprocessed data of quantum-efficiency measurements dependent on wavelength at 610 mK. The results between 800 nm and 1040 nm are dominated by systematic errors and make any determination of a cutoff wavelength impossible.

Temperature [K]	Bias Current [% I_c]	Cutoff Wavelength [nm]
0.61	91.6	1188
0.61	84.2	1006
0.61	78.3	721
0.61	70.9	487
2	94.5	1113
2	89.4	1019
2	82.7	879
2	74.3	411
4	92.4	757
4	83.8	461
4	74.5	365

Table 8: Summary of the cutoff conditions of the TaN-SNSPD resulting from wavelength scans at fixed bias current.

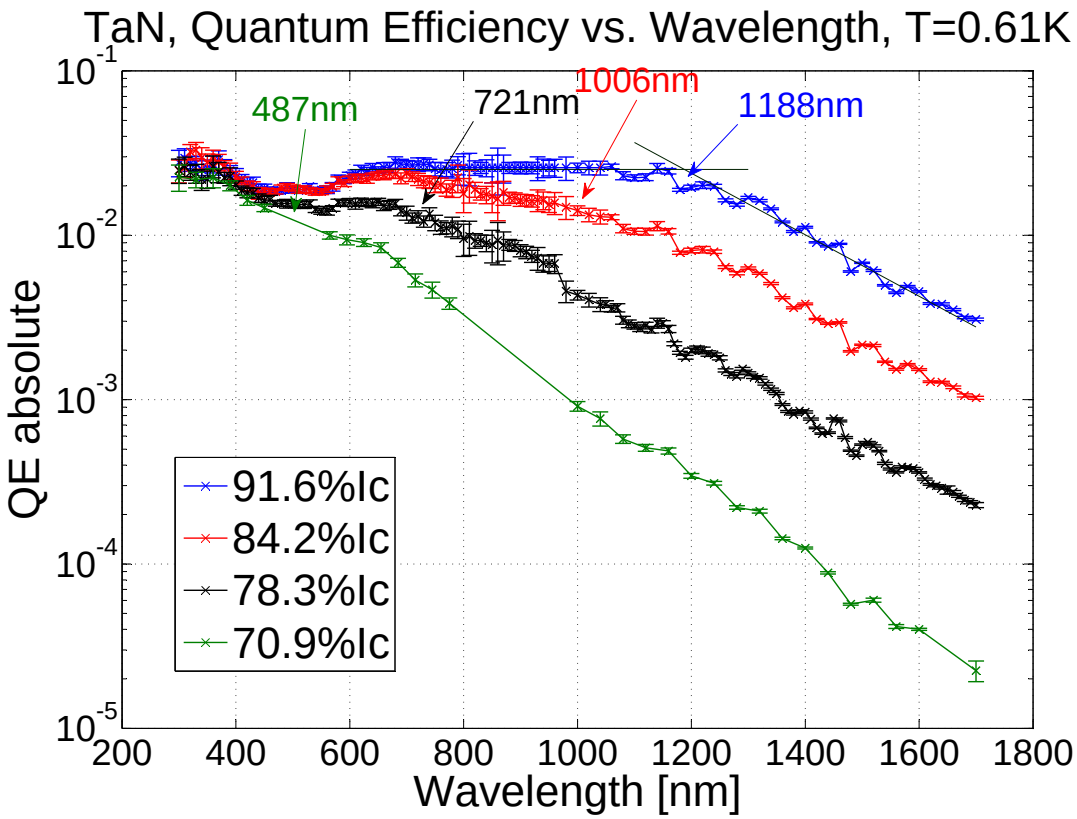

Figure 26: Smoothened results of quantum efficiency dependent on wavelength at 610 mK. The cutoff wavelength was determined by the intersection of two exponential fits and the results are indicated by arrows. The fit-lines are shown for the scan at 91.6% I_c.

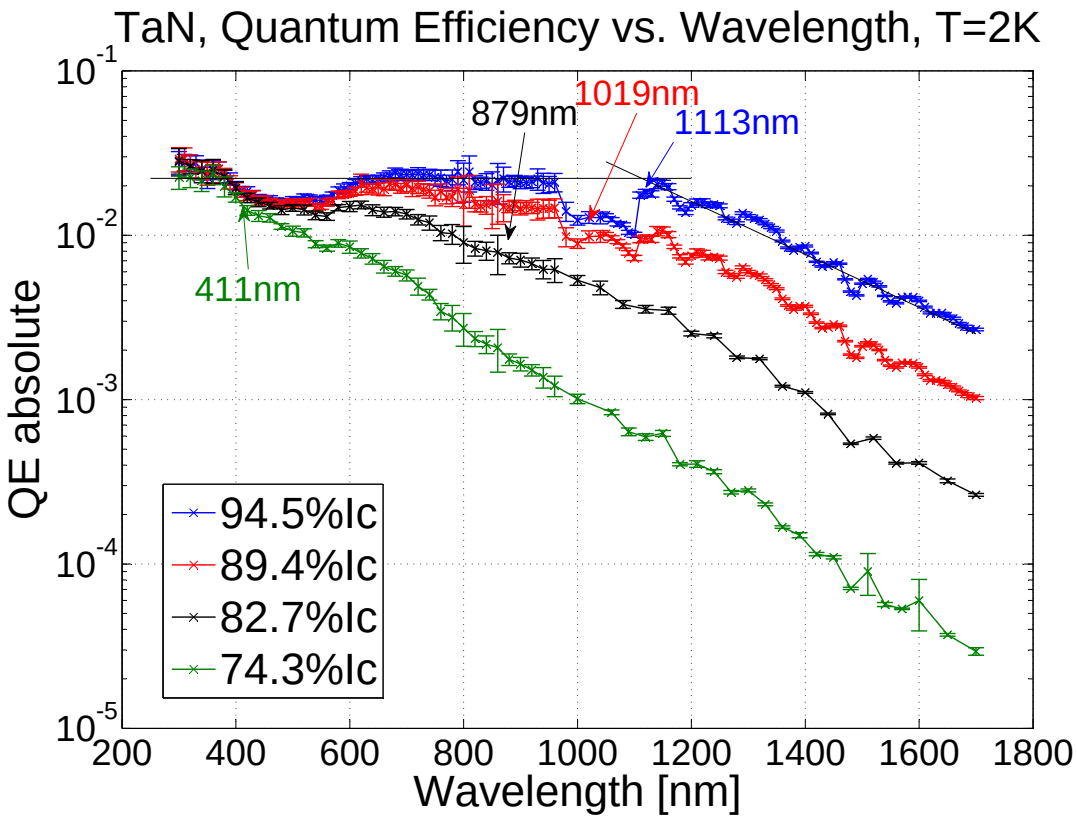

Figure 27: Smoothened results of quantum efficiency dependent on wavelength at 2 K. The cutoff wavelength was determined by the intersection of the two exponential fits and the results are indicated by arrows. The fit-lines are shown for the scan at 94.5% I_c.

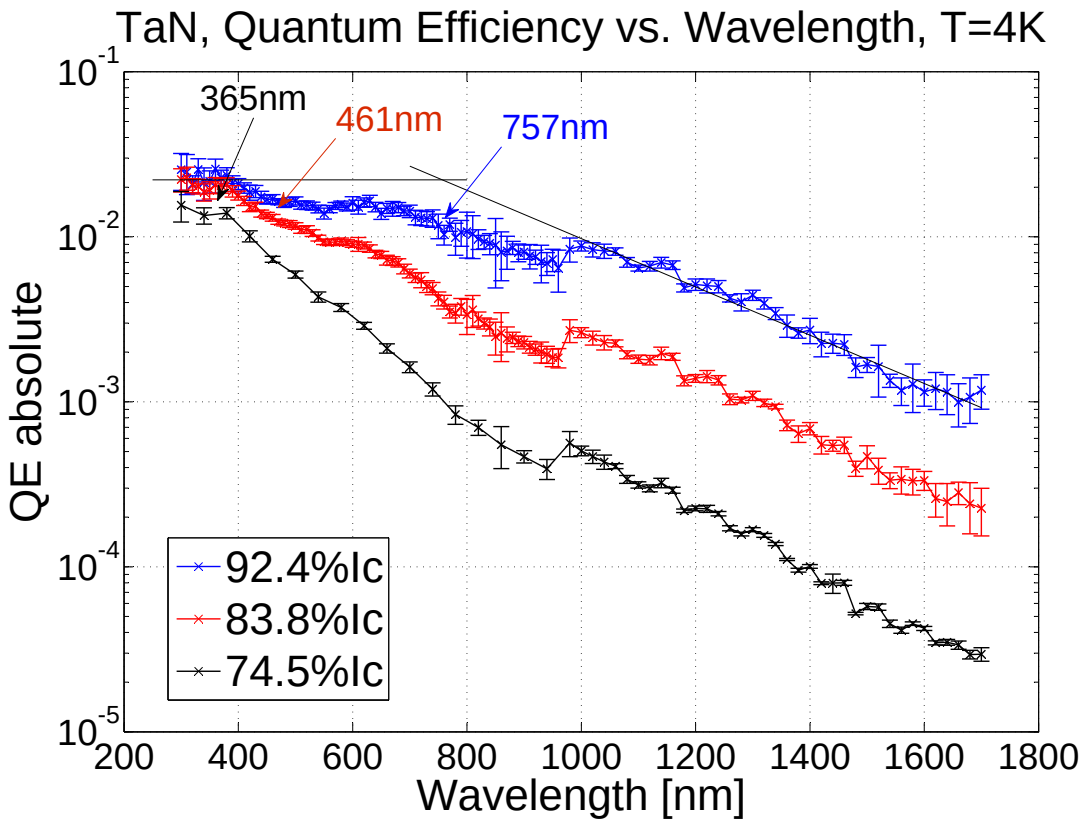

Figure 28: Smoothened results of quantum efficiency dependent on wavelength at 4 K. The cutoff wavelength was determined by the intersection of the two exponential fits and the results are indicated by arrows. The fit-lines are shown for the scan at 92.4% I_c.

5.5 Comparison of Quantum Efficiencies

Looking at the results from section 5.4, in general one can say that the cutoff wavelengths have been increased by the use of TaN. While the cutoff wavelengths of the NbN-SNSPD appear to be in the ultraviolet or visible, the cutoff wavelengths of the TaN-SNSPD have been shifted well into the near-infrared.

A determination of a device quantum-efficiency proves to be very difficult since the bias-current scans and the photon-wavelength scans yield different results. The quantum efficiency at the cutoff of the NbN-SNSPD resulting from the bias-current scans are in the range of 0.3%. The quantum efficiencies resulting from photon-wavelength scans yield 2.6% to 5.5%. The quantum efficiencies of the TaN-SNSPD resulting from the bias-current scans at the cutoff lie between 0.15% and 0.76%. From the photon-wavelength scans of the TaN-SNSPD values between 0.72% and 1.9% could be obtained.

In figure 29 and figure 30 the results from section 5.4 are presented in an overview for the TaN-SNSPD and the NbN-SNSPD. Additionally, the cutoff conditions from the detection model (see Eq.(27)) are plotted as a reference. For the calculation of the cutoff values predicted by the detection model the material parameters from table 1 in section 5.1 and table 2 in section 5.2 have been used. The only free parameter is the quantum yield β, which was chosen as 0.2, a reasonable value for the quantum yield of the quasiparticle multiplication (0.1 after [21]). Changing the quantum yield would move the line for the cutoff condition vertically. The data points in those plots come from both measurement series, the bias scans as well as the wavelength scans.

Looking at figure 29 the data are not to far off the theoretical prediction. Especially the results of the measurements at 0.61 K are in very good agreement. But, contrary to the detection model, the cutoff conditions seem to be somehow dependent on the operation temperature. The lower the temperature the higher the cutoff wavelength (lower the cutoff bias current). Also, the higher the temperature, the worse is the agreement of theory and experiment. A temperature dependent quantum efficiency and therefore temperature dependent cutoff conditions were observed before [4] [27], but there is no conclusive explanation. It seems that the approximative nature of the detection model underestimates a possible influence of the operation temperature, or neglects other influences of the temperature on the system.

The situation in the NbN-system (figure 30) looks different. Here, the measured values do not really correspond to the theoretical prediction. The values for the cutoff condition form an almost straight line. Since the experimental and the theoretical critical-current are much further apart than in the TaN system (see table 3 and 6), a possible overestimation of the bias current with respect to the critical current could account for this puzzling behavior. Looking at the results from the wavelength scans, there seems to be a temperature dependence only for the two data points on the right hand side. The situation is different for the results of the bias scans. Here, like in the TaN system, the cutoff condition seems to be strongly dependent on the operation temperature. The

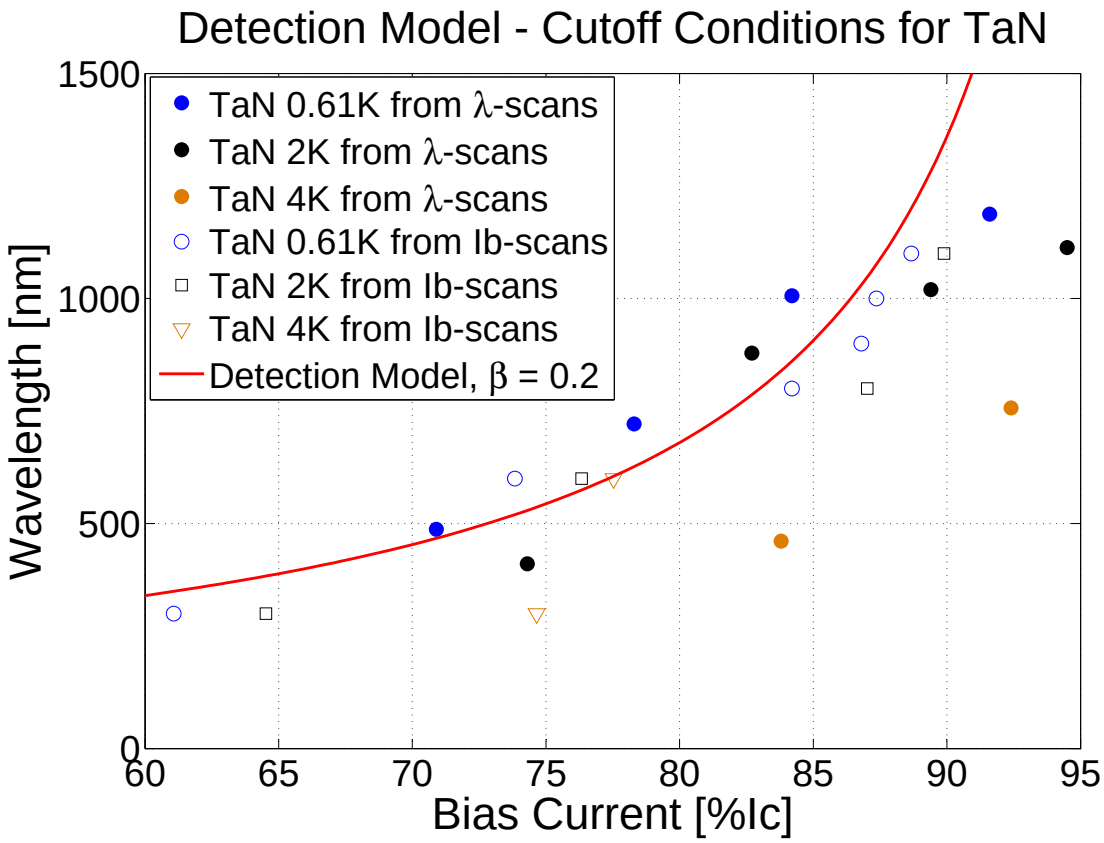

Figure 29: Overview of the cutoff conditions that could be extracted from measurements of the TaN-SNSPD. The closed symbols represent results obtained from wavelength dependent measurements and the open symbols represent results from bias-current scans. The red line indicated the cutoff conditions predicted by the detection model (Eq.(27) in section 3.1). The parameters were taken from table 1 and 2, the value for the quantum yield β was assumed to be 0.2.

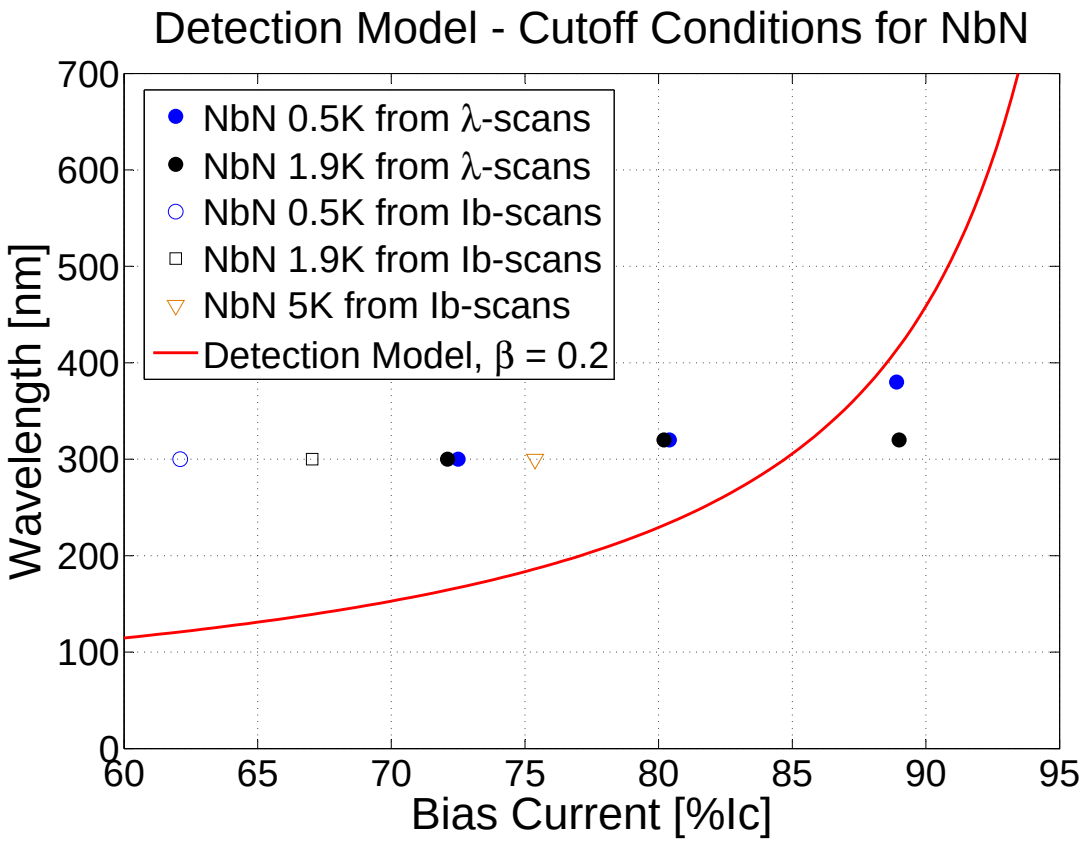

Figure 30: Overview of the cutoff conditions that could be extracted from measurements of the NbN-SNSPD. The closed symbols represent results obtained from wavelength dependent measurements and the open symbols represent results from bias-current scans. The red line indicated the cutoff conditions predicted by the detection model (Eq.(27) in section 3.1). The parameters were taken from table 1 and 2, the value for the quantum yield β was assumed to be 0.2.

determination of the cutoff wavelength from the wavelength scans for both, the TaN- and the NbN-SNSPD, has proven to be rather difficult and also possibly vulnerable to errors. Especially in the NbN-case the regions of saturation are very small and heavily disturbed by systematic errors. The bias-current scans show smoother characteristics and seem to be more reliable. But still, for the NbN bias-scans the change of the slope that defines the cutoff is a lot less pronounced than for the TaN bias-scans. For all NbN-measurements, the results should be treated with care. Systematic errors as well as possible constrictions of the nanowire, and a consequential inaccuracy in the definition of the cutoff condition lead to an uncertainty of the obtained results.

5.6 Dark-Count Measurements

One of the distinct advantages of SNSPDs is the low dark-count rate. To verify that, the dark-count rate has been measured as a function of the bias current. At first, it was the intention to cover the SNSPD with a thermally anchored aluminum cap to ensure that as few photons as possible reach the detector and possibly trigger a fluctuation. A first measurements series was conducted with the TaN-SNSPD. Unfortunately, the data collected were incomprehensive and inconsistent. After this first series of measurements, technical problems with the cryostat made additional measurements impossible.

Still, it is possible to extract some information about the dark-count rate from the count-rate measurements as a function of the bias current. As mentioned in section 5.4, background counts have been measured in order to subtract them from the bias-current dependent count-rate measurements at fixed wavelength. These measurements present a combination of the photon background from the surrounding light and blackbody radiation originating from inside and outside the cryostat as well as the intrinsic fluctuations that are the real dark counts. In section 3.1.1 two fluctuation models have been mentioned. Both these scenarios expect the fluctuation rate to depend strongly on the bias current. For the unbinding of vortex and antivortex pairs the bias current lowers the binding energy, for the vortex entry scenario the bias current lowers the energy barrier for the entry of the vortices. For those measurements that combine background photon counts and fluctuations, the strong bias current dependence means that at low bias currents the counts from the background photons should be dominant, and at higher bias currents the intrinsic fluctuations should become dominant. To have a closer look at the fluctuation data the model proposed by Bulaevskii et al. [22] mentioned in section 3.1.1 as “Single Vortex Entry” was chosen. The model has been fitted to the data acquired at high bias currents when the real fluctuations are expected to be dominant.

According to [22] the analytical expression for the single vortex entry is given by

$$\ln\left(\frac{R}{L\cdot a}\right) = \ln\left[Y\left(\frac{\Phi_0 I}{\pi\nu k_B T}\right)\right], \tag{28}$$

where R is the fluctuation rate, L the length of the nanowire, Φ_0 the magnetic flux

quantum and I the bias current. The second term on the right hand side is

$$\ln\left[Y\left(\frac{\Phi_0 I}{\pi\nu k_B T}\right)\right] = \frac{\nu+1}{2}\ln\left[1+\left(\frac{\Phi_0 I}{\pi\nu k_B T}\right)^2\right] + \frac{\Phi_0 I}{\pi k_B T}\arctan\left(\frac{\pi\nu k_B T}{\Phi_0 I}\right). \quad (29)$$

All variables are known except for a and ν, which are used as fit parameters. The first parameter is given as

$$a = \frac{4k_B T R_\square}{\Phi_0^2 w}\left(\frac{\pi\nu^3}{2}\right)^{\frac{1}{2}}\left(\frac{\pi\xi}{w}\right)^{\nu+1}, \quad (30)$$

where w is the width of the conduction path and $R_\square$ is the sheet resistance for a conduction path with the thickness d that calculates as

$$R_\square = \frac{\rho}{d}. \quad (31)$$

The second fit parameter ν is

$$\nu = \frac{\Phi_0^2(1-\exp(-2))}{2\pi\mu_0\Lambda k_B T}. \quad (32)$$

From Eq.(32) Λ can be calculated and from Eq.(30) the coherence length ξ can be calculated as

$$\xi = \left(\frac{a\Phi_0^2 w}{4k_B T R_\square}\right)^{\frac{1}{\nu+1}}\left(\frac{2}{\pi\nu^3}\right)^{\frac{1}{2(\nu+1)}}\left(\frac{w}{\pi}\right). \quad (33)$$

Figure 31 shows the background measurements of the TaN-SNSPD. The measurements were conducted at three temperatures. The measurements at 610 mK (in blue) and 2 K (in black) show the expected behavior. At very high bias currents there is a steep rise in the count rate coming from the strong bias current dependence of the fluctuations. At low bias currents the photons from the background are dominant. The measurement at 4 K shows a strange behavior. At very low bias currents there is a change in the slope of the curve indicating a similar behavior as in the case of 0.61 K and 2 K. At moderate bias currents (80% - 90% of I_c) the curve gets steeper. That could be the regime dominated by fluctuations. But at very high bias currents the curve flattens again. The reason for that behavior is not absolutely clear. A possible explanation could come from the fact that at a certain point the single fluctuation events are not independent from each other anymore. The independence of each single event is a assumption in all fluctuation-models that is obviously not valid any more at some point. This point could have been reached for the background measurement of the TaN-SNSPD at 4 K.

Equation (28) has been fitted to the data presented in figure 31. The agreement for all data sets is excellent. The fit for the data acquired at 2 K is shown in figure 32

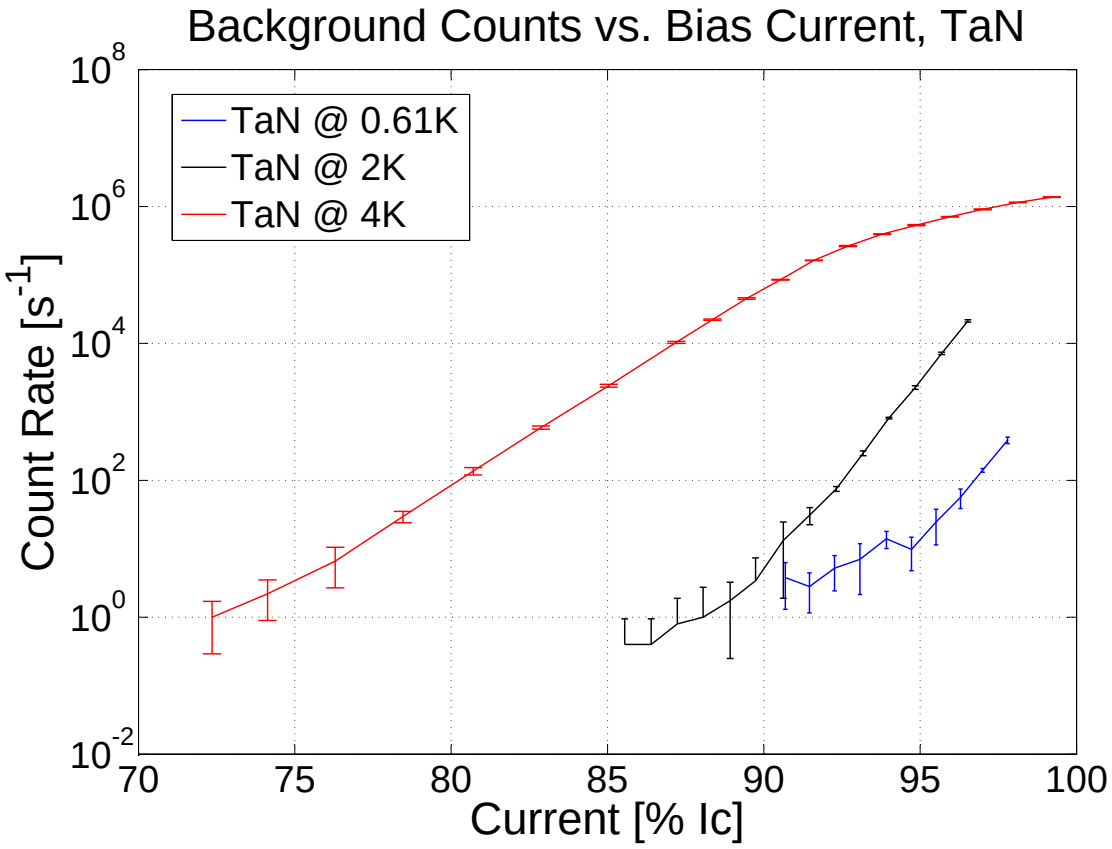

Figure 31: Measurements of the background counts of the TaN-SNSPD as a function of reduced bias current at three temperatures. At low bias-currents the counts from the background photons are dominant. At high bias-currents a steep rise of the count rate sets in. This is due to the fluctuations becoming dominant. The curve at 4 K shows an atypical behavior. See main text for a more detailed discussion.

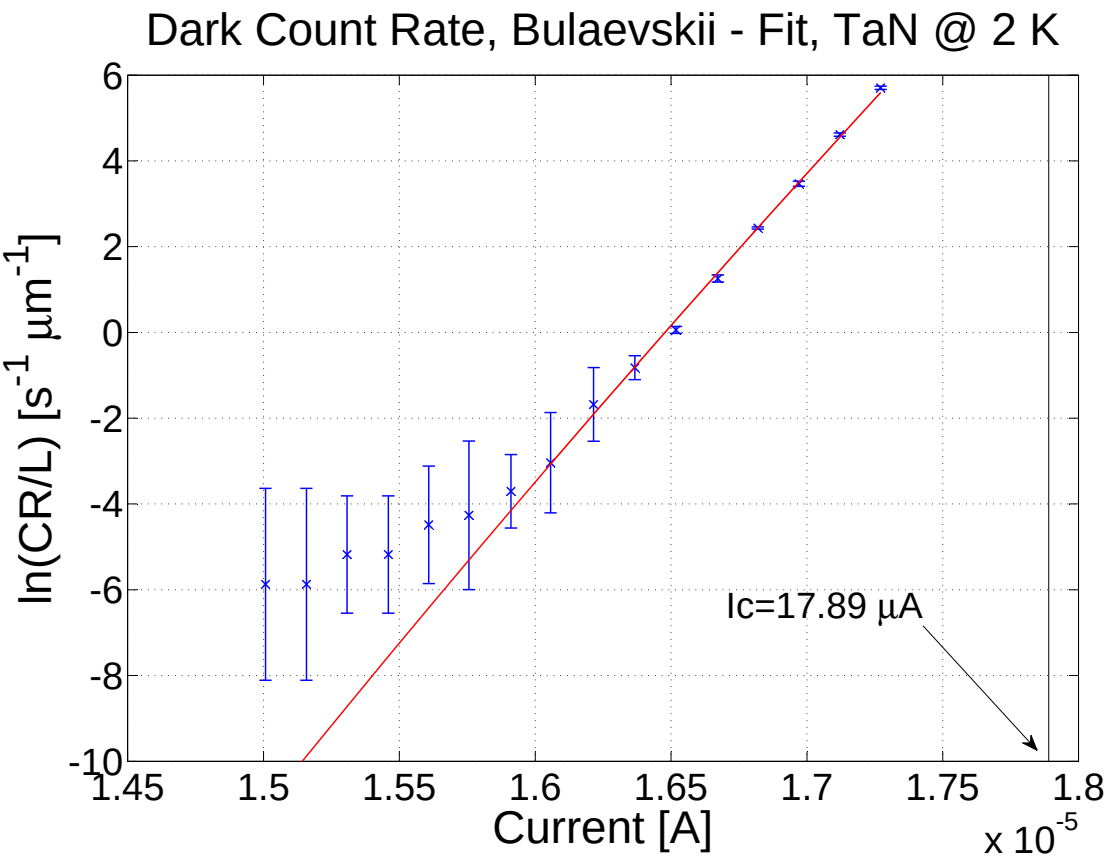

Figure 32: Data of the background count rate of the TaN-SNSPD at 2 K devided by the length of the nanowire on a logarithmic scale. The solid line is the fit of the fluctuation model by Bulaevskii [22] (see also (28)). The critical currents are indicated by the vertical line in black.

exemplarily. Using Eqs.(32) and (33) the physically meaningful parameters ξ and Λ have been calculated from the fit parameters. These results are presented in table 9 and compared with the values derived from the properties in table 1 and 2 using Eqs.(13), (2) and (18). The agreement of the values from the measurements at 2 K and 4 K for Λ is excellent and also for ξ quite good. Only the fit to the measurement at 0.61 K underestimates (overestimates) the value for the coherence length (effective penetration depth) dramatically.

The background measurements of the NbN-SNSPD are a little more problematic to analyze. Figure 33 shows the background count-rate measured at 5 K. The change of the slope to the regime where the real fluctuations become dominant as it was the case for the background measurements of the TaN-SNSPD, is missing. Compared to the

T [K]	$\xi(T)$ [nm]	$\Lambda(T)$ [μm]	ξ_{Fit} [nm]	Λ_{Fit} [μm]
0.6	5.664	129.89	0.8867	430.33
2	6.032	130.96	3.4755	120.78
4	6.976	146.81	3.253	134.56

Table 9: Comparison of the coherence length (ξ) and the effective penetration depth (Λ) obtained from the resistance measurements in magnetic fields (see section 2) to the values obtained by the fit of the dark-count rate to the fluctuation model by Bluaevskii [22].

$\mathbf{T_c}$ [**K**]	**d** [**nm**]	**w** [**nm**]	$\xi(\mathbf{0})$ [**nm**]	$\lambda(\mathbf{0})$ [**nm**]	$\mathbf{\Lambda(0)}$ [μ**m**]	$\mathbf{R_\square}$ [**Ω**]
12.37	6	82.9	4.2	384.7	59.2	395.93

Table 10: Properties of the NbN-SNSPD used by Bartolf et. al [15]. The dark count data of this SNSPD was used in figure 33 and the properties have been used for the fit in figure 34. Also some of the properties in table 11 have been derived from the properties in this table.

background counts of the TaN-SNSPD, the counts caused by background photons in the NbN-SNSPD used for this thesis are two or three orders of magnitude higher. This is because of a change in the experimental setup. When measuring the NbN-SNSPD there was quite a lot of background light from the surrounding incident on the detector (illumination of the lab, reflecting sunlight, 300 K blackbody radiation of the lab). These external influences were unproblematic for the quantum-efficiency measurements as long as they were constant. But for the fluctuation measurements they lead to a much higher background. For the measurements of the TaN-SNSPD, the experimental setup was equipped with a set of aluminum boards that darkened the experiment leading to a much lower background count rate and therefore the fluctuations become dominant at lower bias currents. The high background count rate of the NbN-SNSPD has the consequence that a domination of the real fluctuation would occur at higher bias currents that were not accessed in this measurement. To compare the fluctuations in a NbN-SNSPD with the fluctuation model by Bulaevskii, real fluctuation-data of a different NbN-SNSPD with similar dimensions measured at 5.5 K and published by Bartolf et al. [15] were made use of. This measurement is shown in figure 33. The properties of this SNSPD are published in [15] and summarized in table 10. Because of the similarities of the electronic and geometric properties, we expect a comparable behavior of the SNSPD used for this thesis and the one used in [15]. The two measurements in figure 33 show the same characteristics as the background measurements of the TaN-SNSPD, but instead of combining the two regimes in the same curve, the fluctuations and the background counts are separated.

	T [K]	$\xi(T)$ [nm]	$\Lambda(T)$ [μm]	ξ_{Fit} [nm]	Λ_{Fit} [μm]
Bartolf et. al	5.5	5.141	54	4.326	44.29
This thesis	5	4.799	51.414	-	-

Table 11: Comparison of the coherence length and the effective penetration depth obtained from the resistance measurements in magnetic fields (see section 2) to the values obtained by the fit of the dark-count rate to the fluctuation model by Bluaevskii [22].

Here also, the model from [22] has been fitted to the real fluctuation data measured by Bartolf et. al and the fit is presented in figure 34. The values for ξ and Λ have been extracted in an analog way and compared to the properties determined by the resistance measurements in magnetic fields and the values derived from the properties published in [15]. Those results are shown in table 11. The coherence lengths and the effective penetration depths are in good agreement.

Unfortunately the values of the dark-count rates are difficult to compare since the measurements of the TaN-SNSPD at 4 K shows a strange behavior. The temperatures of the two other measurements are too far off the NbN-measurements, so that a direct comparison does not make much sense. But in both systems the dark-count rates for practical bias currents and operation temperatures are between 10^{-1} Hz and 10^{3} Hz. This is low compared to an InGaAs-APD operated in Geiger mode, for example, with a dark-count rate of a few kHz [2].

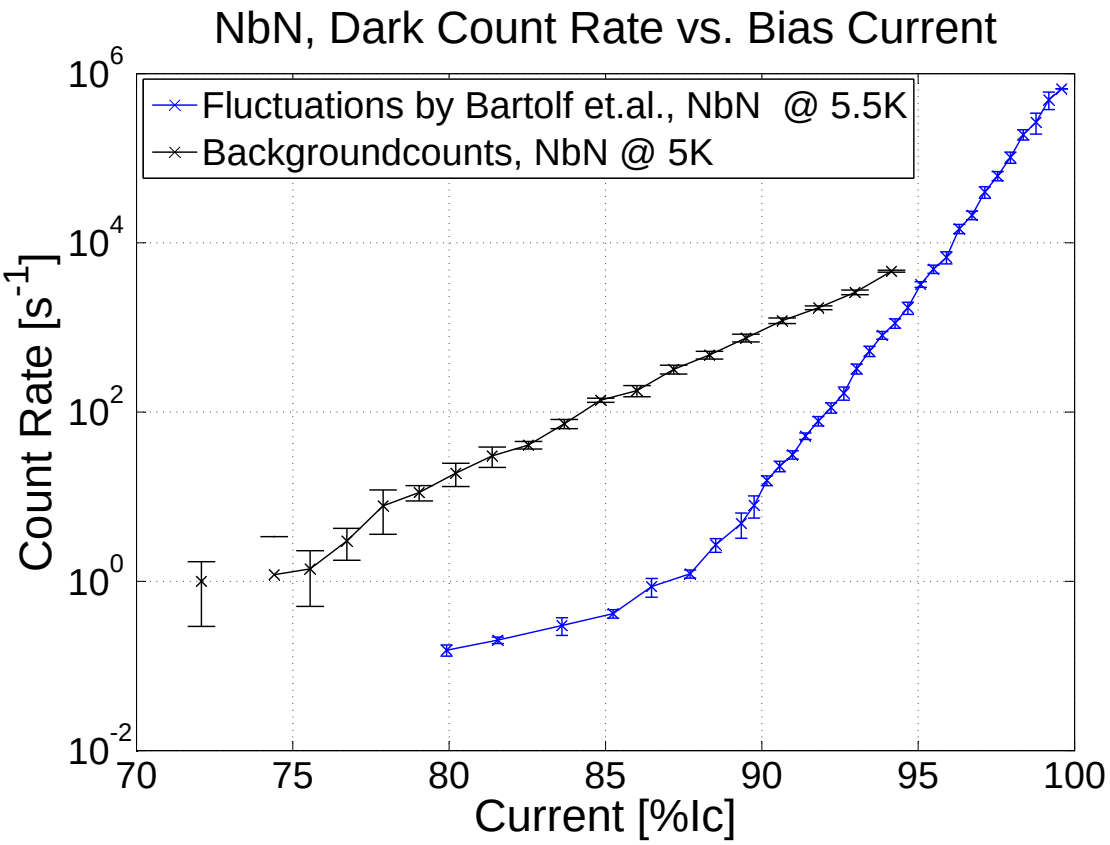

Figure 33: In black: measurements of the background of the NbN-SNSPD used in this thesis at 5 K. In blue: dark count measurements by Bartolf et. al [15] of a NbN-SNSPD with similar properties and geometry.

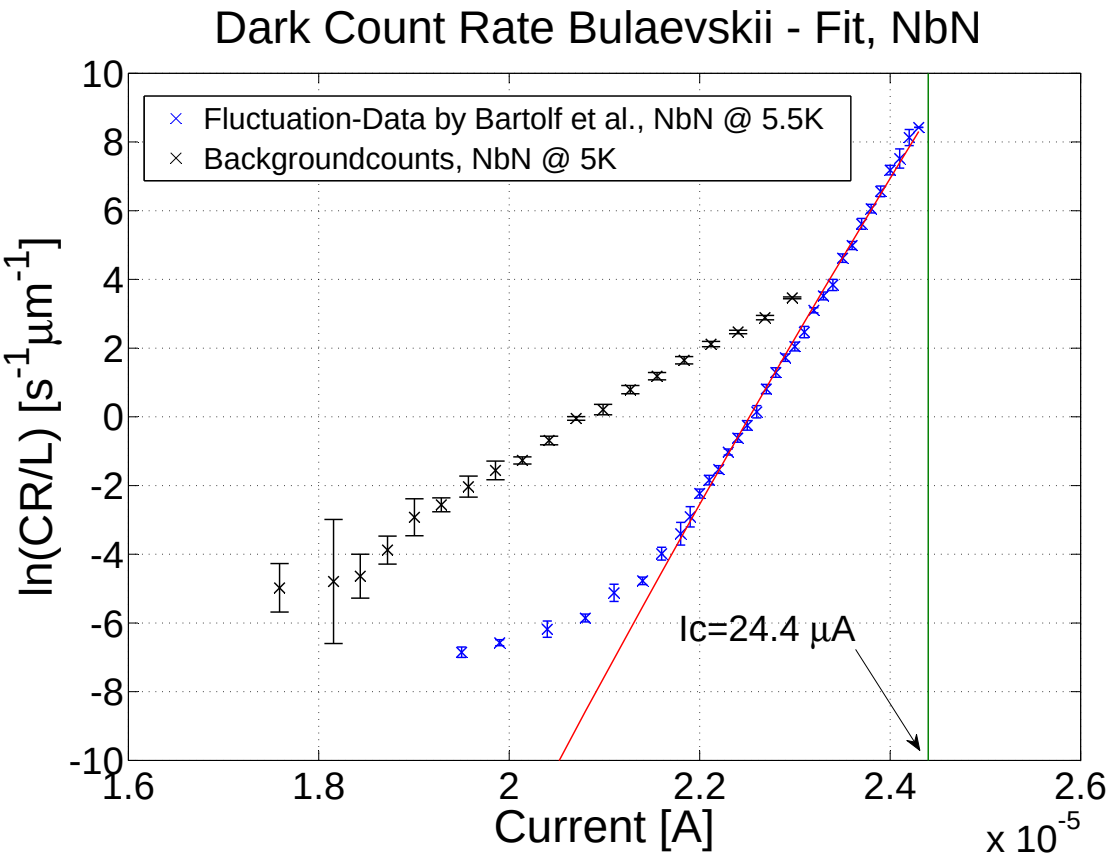

Figure 34: In blue: data of the dark-count rate of a NbN-SNSPD at 5.5 K by Bartolf et. al [15], devided by the length of the nanowire on a logarithmic scale. The solid line is the fit of the fluctuation model by Bulaevskii [22] (see also Eq.(28)). The critical current is indicated by the vertical green line. For completeness the data of the background counts of the NbN-SNSPD used for this thesis at 5 K are also shown in black.

6 Conclusions, Improvements and Outlook

The cutoff conditions of a TaN-SNSPD and a NbN-SNSPD have been measured by means of quantum-efficiency measurements with varying bias current and incident photon wavelength. The cutoff in detection efficiency of the TaN-SNSPD was measured to be at substantially higher wavelengths or lower bias currents as compared to the NbN-SNSPD. Due to large discrepancies of the results for the quantum efficiency between bias-current dependent and photon-wavelength dependent measurements, an absolute value for the quantum efficiency could not be determined. All measurements suffer from high systematic errors. Another source of errors is the calibration of the light source. The measurements show a temperature dependence that is not expected by the detection model. The reasons for that temperature dependence remain unclear, but measurements are under way to shed light on this issue.

Information about the dark counts of the TaN-SNSPD were extracted from background measurements and were compared to a mathematical model that describes these fluctuations. The overall agreement is excellent, and the superconducting properties that can be deduced from the fit parameters agree with the measured properties from resistance measurements in a PPMS-system for 2 K and 4 K. In the case of 610 mK, the properties do not agree any more. To investigate the intrinsic fluctuations of the NbN-SNSPD, fluctuation data of a different SNSPD had to be made use of. The superconducting parameters obtained from fitting the fluctuation model to these data agree quite well with the properties published together with this dataset.

In order to measure a reliable and reproducible quantum efficiency, the systematic errors that are present in every measurement would have to be reduced. To investigate the possible temperature dependence of the cutoff conditions, a profound measurement series of quantum efficiency at many different temperatures could reveal more information about this dependence. Such measurements are carried out at the present time. To reduce the influences of the errors of the calibration values, the optical setup could be changed and simplified in order to reduce possible influences of the polarisation of the light on the calibration. This is in fact already in progress.

As a next step in this project, a further focus will be the detection of X-rays with similar structures, probably based on TaN because of a higher X-ray absorption due to the higher atomic number of Ta.

7 Acknowledgement

I would like to thank Prof. Dr. A. Schilling for giving me the opportunity for this Master Thesis in this interesting project. I would also like to thank Dr. A. Engel for welcoming me to the photon-detection group and most of all for continuous support, help and advice during the entire time of this thesis. Further I thank Dr. H. Bartholf and K. Inderbitzin for the constant willingness for discussion, and inputs they have given me.

References

[1] A. Semenov, A. Engeland, K. Il'in, G. Gol'tsman, M. Siegel, and H.-W. Hübers, "Ultimate performance of a superconducting quantum detector," *Eur. Phys. J. AP*, vol. 21, no. 3, pp. 171 – 178, 2003.

[2] A. Tosi, A. Dalla Mora, F. Zappa, S. Cova, M. A. Itzler, and X. Jiang, "InGaAs/InP Single-Photon Avalanche Diodes show low dark counts and require moderate cooling," *SPIE*, vol. 7222, 2009.

[3] M. Hofherr, D. Rall, K. S. Il'in, A. Semenov, H.-W. Hübers, and M. Siegel, "Superconducting nanowire single-photon detectors: Quantum efficiency vs. film thickness," *Journal of Physics: Conference Series*, 2010.

[4] T. Yamashita, S. Miki, W. Qiu, M. Fujiwara, M. Sasaki, and Z. Wang, "Temperature Dependent Performances of Superconducting Nanowire Single-Photon Detectors in an Ultralow-Temperature Region," *Applied Physics Express*, vol. 3, p. 102502, 2010.

[5] I. Milostnaya, A. Korneev, I. Rubtsova, V. Seleznev, O. Minaeva, G. Chulkova, O. Okunev, B. Voronov, K. Smirnov, G. Gol'tsman, W. Slysz, M. Wegrzecki, M. Guziewicz, J. Bar, M. Gorska, A. Pearlman, J. Kitaygorsky, A. Cross, and R. Sobolewski, "Superconducting single-photon detectors designed for operation at 1.55-μm telecommunication wavelength," *Journal of Physics: Conference Series*, vol. 43, pp. 1334 – 1337, 2006.

[6] R. H. Hadfield, "Single-photon detectors for quantum information applications," *Nature Photonics*, vol. 3, pp. 696–705, 2009.

[7] A. D. Semenov, G. N. Gol'tsman, and A. A. Korneev, "Quantum detection by current carrying superconducting film," *Physica C*, vol. 351, pp. 349–356, 2001.

[8] G. N. Gol'tsman *et al.*, "Ultrafast superconducting single-photon detectors for near-infrared-wavelength quantum communication," *Phys. Stat. Sol. (c)*, vol. 2, no. 5, 2005.

[9] K. M. Rosfjord *et al.*, "Nanowire Single-photon detector with an integrated optical cavity and anti-reflection coating," *Optics Express*, vol. 14, no. 2, p. 527, 2006.

[10] W. Buckel and R. Kleiner, *Superconductivity*, 2nd ed. Germany: Wiley-VCH Verlag GmbH, Weinheim, 2004.

[11] M. Tinkham, *Introduction to Superconductivity*, 2nd ed. United States of America: McGraw-Hill, Inc., New York, 1996.

[12] H. Bartolf, "Fabrication and Characterization of Superconducting Nanowire High-speed Single-Photon Detectors," Ph.D. dissertation, Universität Zürich, 2010.

[13] R. Romestain, B. Delaet, P. Renaud-Goud, I. Wang, C. Jorel, J.-C. Villegier, and J.-P. Poizat, "Fabrication of a Superconducting Niobium Nitride Hot Electron Bolometer for Single-Photon Counting," *New J. Phys.*, vol. 6, p. 129, 2004.

[14] N.R.Werhammer, E. Helfand, and P.C.Hohenberg, " Temperature and Purity Dependence of the Superconducting Critical Field, H_{c2}. III. Electron Spin and Spin-Orbit Effects," *Physical Review*, vol. 147, no. 1, p. 295, 1966.

[15] H. Bartolf, A. Engel, A. Schilling, K. Il'in, M. Siegel, H.-W. Hübers, and A. Semenov, "Current-assisted thermally activated flux liberation in ultrathin nanopatterned NbN superconducting meander structures," *Physical Review B*, vol. 81, 2010.

[16] J. Pearl, "Current Distribution in Superconducting Films Carrying Quantized Fluxoids," *Appl. Phys. Lett.*, vol. 5, p. 65, 1964.

[17] K. D. Irwin and G. C. Hilton, *Cryogenic Particle Detection.* Springer, 2005, ch. 3.

[18] B. Cabrera, "Introduction to TES Physics," *J. Low Temp. Phys.*, vol. 151, pp. 82 – 93, 2008.

[19] S. Friedrich, "Superconducting Tunnel Junction Photon Detectors: Theory and Application," *Journal of low Temperature Physics*, vol. 151, pp. 277 – 286, 2008.

[20] P. Lerch and A. Zehnder, *Cryogenic Particle Detection*, ser. Topics in Applied Physics. Germany: Springer, Berlin, 2005, vol. **99**, ch. *Quantum Giaever Detectors: STJ's*, pp. 217 – 267, Edited by Ch. Enss.

[21] A. Semenov, A. Engel, H.-W. Hübers, K. Il'in, and M. Siegel, "Spectral cut-off in the efficiency of the resistive state formation caused by absorption of a single-photon in current-carrying superconducting nano-strips," *Eur. Phys. J. B*, vol. 47, pp. 495–501, 2005.

[22] L. N. Bulaevskii, M. J. Graf, C. D. Batista, and V. G. Kogan, "Vortex-induced dissipation in narrow current-biased thin-film superconducting strips," *Physical Review B*, vol. 83, 2011.

[23] http://www.newport.com, September 2011.

[24] H. Bartolf, K. Inderbitzin, L. B. Gómez, A. Engel, and A. Schilling, "Nanoscale fabrication by intrinsic suppression of proximity-electron exposures and general considerations for easy and effective top-down fabrication," *Journal of Micromechanics and Microengineering*, vol. 20, p. 125015, 2010.

[25] Y. Pellam, G. Dousselin, and J. Pinel, "Temperature and Magnetic Field Dependence of NbN Film Resistivity," *Journal of Low Temperature Physics*, vol. 78, no. 1/2, pp. 63 – 77, 1990.

[26] J.-H. Tyan and T. Lue, "Grain boundery scattering in the normal state resistivity of superconducting NbN thin films," *Journal of Applied Physics*, vol. 75, no. 1, pp. 325 – 331, 1994.

[27] G. Chulkova, I. Milostnaya, A. Korneev, O. Minaeva, I. Rubtsova, B. Voronov, O. Okunev, K. Smirnov, G. Gol'tsman, J. Kitaygorsky, A. Cross, A. Pearlman, R. Sobolewski, and W. Slysz, "Superconducting nanostructures for counting of single photons in the infrared range," in *Advanced Optoelectronics and Lasers, 2005. Proceedings of CAOL 2005. Second International Conference on*, vol. 2, sept. 2005, pp. 100 – 103 vol. 2.

[28] A. Engel, A. Semenov, H.-W. Hübers, K. Il'in, and M. Siegel, *Electric Noise and Local Photon-Induced Nonequilibrium States in a Current-Carrying Nanostructured Superconductor*. Nova Science Publishers, Inc., 2006, ch. 6.

[29] E. Helfand and N. R. Werthamer, "Temperature and Purity Dependence of the Superconducting Critical Field, H_{c2}," *Phys. Rev. Lett.*, vol. 13, pp. 686 – 688, 1964.

[30] A. Semenov, B. Günther, U. Böttger, H.-W. Hübers, H. Bartolf, A. Engel, A. Schilling, K. Il'in, M. Siegel, R. Schneider, D. Gerthsen, and N. A. Gippius, "Optical and Transport Properties of Ultra-Thin NbN Films and Nanostructures," *Phys. Rev. B*, vol. 80, p. 054510, 2009.

[31] I. Milostnaya, A. Korneev, M. Tarkhov, A. Divochiy, O. Minaeva, V. Seleznev, N. Kaurova, B. Voronov, O. Okunev, G. Chulkova, K. Smirnov, and G. Gol'tsman, "Superconducting Single Photon Nanowire Detectors Development for IR and THz Applications," *Journal of Low Temperature Physics*, vol. 151, pp. 591 – 596, 2008.